# Charge-Transfer States of Bridged Transition Metal Dimers: Mono- vs Binuclear Copper Azide Systems with Relevance to Oxy-Hemocyanin

**Felix Tuczek[†] and Edward I. Solomon[*]**

Department of Chemistry, Stanford University, Stanford, California 94305

*Received December 4, 1992*

The charge-transfer (CT) spectra of transition metal complexes show characteristic changes upon dimer formation. This study focuses on the $(\pi^{nb}) \rightarrow$ Cu CT transitions of Cu azide systems which each split into two transitions if coordination to one copper center is replaced by bridging to two copper centers. In addition, a shift of the in-plane $(\pi^{nb})_\sigma \rightarrow$ Cu CT transitions of the azide systems to lower energy is observed in the dimer spectrum. This shift is ascribed to a strong antiferromagnetic interaction in the CT excited state which is due to coupling of one electron in the bridging orbital with one unpaired electron on a copper center. Three models are developed and evaluated to interpret these CT excited-state shifts and splittings. The excitonic model evaluates only the diagonal energies (i.e. within the CT state) and gives a splitting scheme known from exciton theory which describes the dimer coupling in terms of four two-electron parameters. As the CT state splittings given by this model are too small, off-diagonal terms have to be considered. This is done in terms of molecular orbital (MO model) and valence-bond (VB) theory (VBCI model). It is shown that the VBCI model accounts for the sign and magnitude of the CT state splitting observed in Cu azide systems. In terms of this model, excited-state antiferromagnetism is described as configuration interaction (CI) with metal → metal CT (MMCT) and double CT (DCT) states. It is further shown that the VB and MO models agree in the description of triplet CT states and that the triplet CT state splitting corresponds to the HOMO–LUMO splitting of the dimeric complex. In order to obtain quantitative information regarding the CT transition energies and splittings, SCF–X$\alpha$ SW calculations are performed on a structurally characterized Cu azide monomer and dimer. The implications of the excited-state interactions on the ground-state properties of bridged dimers are discussed.

## I. Introduction

The electronic structure of transition metal dimers has been of continued interest in bioinorganic and magnetochemistry, materials science, and solid-state physics.[1,2] Theoretical analysis of these systems has mainly focused on a quantitative description and computation of ground-state properties, in particular the exchange coupling constant $J$.[3] In contrast, the dimer interactions present in excited electronic states have been investigated in a less systematic way. Notable exceptions are magnetic interactions in excited ligand field (LF) states of certain transition metal pairs which have been studied and analyzed in terms of the Tanabe mechanism.[4] In a copper dimer, a more general picture of the exchange interactions involved in the shifts and splittings of the monomer LF into dimer transitions has been obtained.[5] A comparable understanding of dimer interactions in charge-transfer (CT) states is still lacking.

Evidence for the influence of dimer formation on the CT spectrum of transition metal complexes has been known for some time. Bands with intensities typical of CT transitions which appear in the optical spectra of dimers but are absent in the spectrum of the corresponding monomer have been termed "dimer bands".[6-9] The origin of these transitions has been unclear. A more systematic investigation of these phenomena has been prompted by the effort to interpret the optical spectrum of oxy-hemocyanin (oxy Hc).[10] Hc, the oxygen transport protein of invertebrates, contains a coupled binuclear cupric site which reversibly binds oxygen as peroxide. An analysis of the CT spectrum shows that peroxide bridges the two copper(II)'s,[10] and resonance Raman spectroscopy indicates that peroxide is bound symmetrically.[11] Molecular orbital theory predicts that the dominant bonding interaction in Cu peroxide systems is between the peroxide in-plane $\pi^*_\sigma$ antibonding orbital and the Cu $d_{x^2-y^2}$ orbital and that a much weaker interaction exists between the peroxide $\pi^*_v$ orbital perpendicular to the Cu–$O_2$–Cu plane and the Cu d orbitals.[12] In agreement with this bonding description, two peroxide → Cu transitions are observed in the optical absorption spectrum of a copper peroxo monomer, $[Cu_2(XYL\text{–}O\text{–})O_2]^+$,[13] one high-intensity $\pi^*_\sigma \rightarrow d_{x^2-y^2}$ transition at 19 900 $cm^{-1}$ ($\epsilon$ = 6300 $M^{-1}$ $cm^{-1}$) and one $\pi^*_v \rightarrow d_{x^2-y^2}$ transition at 16 000 $cm^{-1}$ of lower

* Author to whom correspondence should be addressed.
† Present address: Institut für Anorganische und Analytische Chemie, Johannes Gutenberg Universität Mainz, D-6500 Mainz, FRG.

(1) (a) *Magneto-Structural Correlations in Exchange Coupled Systems*; Willett, R. D., Gatteschi, D., Kahn, O., Eds.; Reidel: Dordrecht, The Netherlands, 1985. (b) *Extended Interactions between Metal Ions in Transition Metal Complexes*; Interrante, L. V., Ed.; American Chemical Society: Washington, DC, 1974. (c) *Metal Clusters in Proteins*; Que, L., Ed.; ACS Symposium Series 372; American Chemical Society: Washington, DC, 1988.
(2) Solomon, E. I.; Baldwin, M. J.; Lowery, M. D. *Chem. Rev.* **1992**, *92*, 521–542.
(3) (a) Hatfield, W. E. In ref 1b, pp 108–141. (b) Kahn, O. In ref 1a, pp 37–56.
(4) (a) McClure, D. S. *J. Chem. Phys.* **1963**, *39*, 2850–2855. (b) Lohr, L. L.; McClure, D. S. *J. Chem. Phys.* **1968**, *49*, 3516–3521. (c) Ferguson, J.; Guggenheim, H. J.; Tanabe, Y. *J. Phys. Soc. Jpn.* **1966**, *21*, 692–704. (d) Decurtins, S.; Güdel, H. U. *Inorg. Chem.* **1982**, *21*, 3598–3606 and references therein.
(5) Ross, P. K.; Allendorf, M. D.; Solomon, E. I. *J. Am. Chem. Soc.* **1989**, *111*, 4009–4021.
(6) Hansen, A. E.; Ballhausen, C. J. *Trans. Faraday Soc.* **1965**, *61*, 631–639.
(7) Lever, A. B. P. *Inorganic Electronic Spectroscopy*; Elsevier: New York, 1984.
(8) Dubicki, L. *Aust. J. Chem.* **1972**, *25*, 1141–1149.
(9) (a) Schugar, H. J.; Rossman, G. R.; Barraclough, C. G.; Gray, H. B. *J. Am. Chem. Soc.* **1972**, *94*, 2683–2690. (b) Schugar, H. J.; Rossman, G. R.; Thibeault, J.; Gray, H. B. *Chem. Phys. Lett.* **1970**, *6*, 26.
(10) Eickman, N. C.; Himmelwright, R. S.; Solomon, E. I. *Proc. Natl. Acad. Sci. U.S.A.* **1979**, *76*, 2094–2098.
(11) (a) Larrabee, J. A.; Spiro, T. G. *J. Am. Chem. Soc.* **1980**, *102*, 4217–4223. (b) Freedman, T. B.; Loehr, J. S.; Loehr, T. M. *J. Am. Chem. Soc.* **1976**, *98*, 2809–2815.
(12) Solomon, E. I. In ref 2c, pp 116–150.
(13) The ligand XYL–O contains two tridentate bis(2-pyridylethyl)amine donor units connected by 2-hydroxy-*m*-xylyl. (a) Karlin, K. D.; Cruse, R. W.; Gultneh, Y.; Farooq, A.; Hayes, J. C.; Zubieta, J. *J. Am. Chem. Soc.* **1987**, *109*, 2669–2679. (b) Karlin, K. D.; Cruse, R. W.; Gultneh, Y.; Hayes, J. C.; Zubieta, J. *J. Am. Chem. Soc.* **1984**, *106*, 3372–3374.

0020-1669/93/1332-2850$04.00/0 

intensity ($\epsilon$ = 1100 $M^{-1}$ $cm^{-1}$).[14] However, the optical spectrum of oxy Hc contains *three* dominant absorption features which have been interpreted as peroxide → Cu CT transitions, two bands in the optical absorption spectrum at 17 200 $cm^{-1}$ ($\epsilon$ = 1000 $M^{-1}$ $cm^{-1}$) and 29 000 $cm^{-1}$ ($\epsilon$ = 20 000 $M^{-1}$ $cm^{-1}$) and one absorption feature in the CD spectrum near 480 nm ($\Delta\epsilon$ = 1 $M^{-1}$ $cm^{-1}$).[10] Therefore, a splitting of the monomer CT bands occurs upon bridging in a dimer.

From group theory, every monomer CT transition corresponds to two CT transitions in the dimer, the symmetric and antisymmetric combination of CT transitions to each Cu. The only direct experimental evidence for this splitting has been obtained in a comparative spectroscopic study of monomeric and dimeric Cu azide systems.[15] The HOMO of azide is nonbonding (nb) and doubly degenerate. Upon binding to Cu, it splits into $(\pi^{nb})_\sigma$ and $(\pi^{nb})_v$ the same way as $\pi^*(O_2^{2-})$; Cu azide systems may therefore serve as spectroscopic analogues of Cu peroxide systems. In an end-on azide coordinated Cu monomer, the $(\pi^{nb})_\sigma$ → Cu $d_{x^2-y^2}$ transition is observed at 25 500 $cm^{-1}$ ($\epsilon$ = 2000 $M^{-1}$ $cm^{-1}$). This transition splits in a cis $\mu$-1,3-bridged azide dimer, $[Cu_2(L\text{–Et})N_3]$,[16] into two transitions at 27 400 $cm^{-1}$ ($\epsilon$ = 2100 $M^{-1}$ $cm^{-1}$) and 23 800 $cm^{-1}$ ($\epsilon$ = 1000 $M^{-1}$ $cm^{-1}$). Since a nearly identical spectrum is observed for met-$N_3$-Hc it was concluded that azide is bound symmetrically in a cis $\mu$-1,3 (end-on) fashion by met Hc. In order to account for the observed intensities and splittings of the peroxide and azide → Cu CT bands, a transition dipole vector coupling (TDVC) model has been developed. In terms of this model, the observed splitting is given by the interaction energy of the transition dipoles centered at the two monomer subunits. From the observed intensities of the transitions, CT splittings were obtained which were, however, 1 order of magnitude smaller than the experimental values.[15] Application of the TDVC concept to the optical spectrum of oxy Hc produced splittings and selection rules compatible with a spectroscopically effective model involving a cis $\mu$-1,2 binding geometry of peroxide, in analogy to $\mu$-1,3-azide binding.[10] However, only end-on binding modes were considered.

In order to gain further insight into the electronic structure changes associated with a variation of the peroxide binding mode, the first side-on ($\mu$-$\eta^2$:$\eta^2$) peroxide bridged transition metal dimer, $[Cu(HB(3,5\text{-}i\text{-}Pr_2pz)_3)]_2(O_2))$[17] and the first structurally characterized trans $\mu$-1,2 peroxide bridged Cu dimer, $[(CuL)_2O_2]$,[18] have been investigated spectroscopically.[19,20] These studies support a side-on peroxide-bridged model for the active site of oxy Hc. In addition, broken symmetry SCF–X$\alpha$-SW calculations have been performed on the structurally characterized peroxide–Cu(II) systems, i.e. the monomer, the trans end-on dimer, and the $\mu$-$\eta^2$:$\eta^2$ side-on dimer, and two hypothetical systems, the cis $\mu$-1,2 dimer and the side-on monomer.[21] In accordance with the bonding concept described above, the dominant bonding interaction in all systems is shown to be the $\sigma$ donor interaction between the peroxide $\pi^*_\sigma$ orbital and the copper $d_{x^2-y^2}$ orbitals, with an additional $\pi$ acceptor interaction between the peroxide $\sigma^*$ orbital and the copper $d_{x^2-y^2}$ orbitals in the side-on dimer. Moreover, ground-state coupling constants $J$ as well as optical transition energies have been calculated. With respect to CT transitions, the calculated value of the $\pi^*_v$ → Cu transition energy was always close to the experimental values whereas serious disagreement with the spectroscopic data was noted with respect to the calculated $\pi^*_\sigma$ → Cu CT transition energy in the dimer systems, which was consistently much greater than observed experimentally. In order to understand the origin of the disagreement between the calculated and observed $\pi^*_\sigma$ CT energies, the interactions present in excited electronic states of dimers have to be considered in more detail.

In copper acetate, the shift and splitting of each LF monomer transition into four dimer transitions can be expressed in terms of four parameters.[5] The Coulomb integral $K$ accounts for an overall shift of the dimer transitions with respect to the parent monomer transition. The exchange integral $J$ determines the magnitude of the excited-state singlet–triplet splitting. In contrast to the ground state, excited LF states are further split by the "Coulomb mediated excitation transfer integral" $I$ and the "exchange mediated excitation transfer integral" $L$.[22,23] This description has been extended to the peroxide → Cu and the azide → Cu CT spectra in oxy Hc and the mentioned series of azide-bridged dimers, respectively. As the part of the splitting described by $I$ is exactly the splitting as calculated by the TDVC model, the mentioned discrepancy between the observed CT transition splittings and the values obtained with the TDVC model were therefore ascribed to the neglect of $L$.[15] Similarly, the discrepancy between the $\pi^*_\sigma$ → Cu CT transition energies calculated with the SCF–X$\alpha$ method and those observed for the trans and side-on Cu peroxo dimers was ascribed to the influence of the excited-state exchange integrals, in particular the magnetic coupling constant $J$, which have not been taken into account in the calculation.[21] Since, for a $\pi^*_\sigma$ CT state, a single electron in the bridging ligand orbital interacts with a single electron in one Cu centered orbital with large overlap, a very strong antiferromagnetic CT excited-state magnetic exchange interaction results which is much stronger than the ground-state $J$ and may lower the energy of the singlet CT state appreciably (i.e. by thousands of $cm^{-1}$).[24]

In order to obtain a more quantitative understanding of CT state shifts and splittings, a theoretical study is performed on a structurally characterized Cu cis $\mu$-1,3 azide dimer $[Cu_2(L\text{–Et})N_3]$ and a corresponding monomer. As already mentioned, these are the only systems where an unambigous experimental splitting of a monomer CT transition in a dimer has been obtained. Three models are presented and compared to explain the experimental findings. The excitonic model which involves the $I$, $J$, $K$, and $L$ integrals is parallel to the model applied for d–d transitions in Cu acetate and is shown to give too small splittings in CT states. Starting from the excitonic model, two alternative approaches are presented, the valence-bond configuration interaction (VBCI) model and the molecular orbital (MO) model. It is shown that both models agree in the description of triplet CT states but differ in the description of singlet CT states. In the framework of the MO model, broken and full symmetry SCF–X$\alpha$-SW ground- and transition-state calculations are performed on the azide monomer and dimer. The results of these calculations are compared with the predictions of the VBCI model and spectroscopic data. Finally, the relationship of the excited-state

(14) Pate, J. E.; Cruse, R. W.; Karlin, K. D.; Solomon, E. I. *J. Am. Chem. Soc.* **1987**, *109*, 2624–2630.
(15) Pate, J. E.; Ross, P. K.; Thamann, T. J.; Reed, C. A.; Karlin, K. D.; Sorrell, T. N.; Solomon, E. I. *J. Am. Chem. Soc.* **1989**, *111*, 5198–5208.
(16) The ligand L–Et is the anion of *N,N,N',N'*-tetrakis[2-(1-ethylbenzimidazolyl)]-2-hydroxy-1,3-diaminopropane: McKee, V.; Zvagulis, M.; Dagdigian, J. V.; Patch, M. G.; Reed, C. A. *J. Am. Chem. Soc.* **1984**, *106*, 4765–4772.
(17) The ligand $HB(3,5\text{-}iPr_2pz)_3$ is hydridotris(3,5-diisopropylpyrazolyl)borate: (a) Kitajima, N.; Fujisama, K.; Moro-oka, Y.; Toriumi, K. *J. Am. Chem. Soc.* **1989**, *111*, 8975–8976. (b) Kitajima, N.; Koda, T.; Hashimoto, S.; Kitagawa, T.; Moro-oka, Y. *J. Chem. Soc., Chem. Commun.* **1988**, *110*, 3690–3692.
(18) The ligand L is tris[(2-pyridyl)methyl]amine: Jacobson, R. R.; Tyeklár, Z.; Farooq, A.; Karlin, K. D.; Liu, S.; Zubieta, J. *J. Am. Chem. Soc.* **1988**, *110*, 3690–3692.
(19) Baldwin, M. J.; Ross, P. K.; Pate, J. E.; Tyeklár, Z.; Karlin, K. D.; Solomon, E. I. *J. Am. Chem. Soc.* **1991**, *113*, 8671–8679.
(20) Baldwin, M. J.; Root, D. E.; Pate, J. E.; Fujisawa, K.; Kitajima, N.; Solomon, E. I. *J. Am. Chem. Soc.* **1992**, *114*, 10421–10431.
(21) Ross, P. K.; Solomon, E. I. *J. Am. Chem. Soc.* **1991**, *113*, 3246–3259.
(22) Craig, D. P.; Walmsley, S. H. *Excitons in Molecular Crystals*; Benjamin: New York, 1968.
(23) (a) Kasha, M.; Rawls, H. R.; El-Bayoumi, M. A. *Pure Appl. Chem.* **1965**, *11*, 371–392. (b) Tanabe, Y.; Aoyagi, K. In *Excitons*; Rashba, E. I., Sturge, M. D., Eds.; North-Holland: Amsterdam, The Netherlands, 1982; pp 603–663.
(24) Desjardins, D. R.; Wilcox, D. E.; Musselman, R. L.; Solomon, E. I. *Inorg. Chem.* **1987**, *26*, 288.

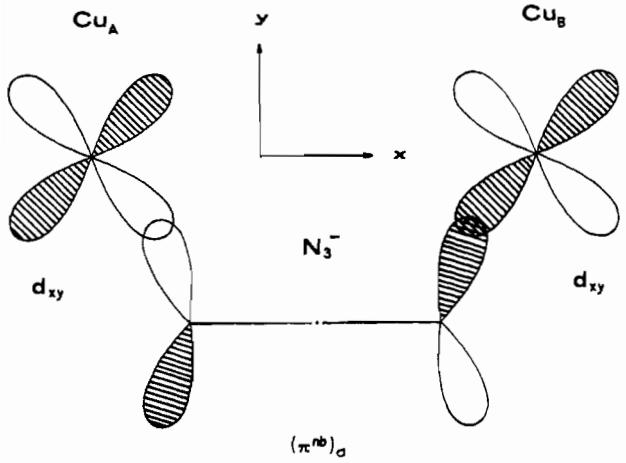


**Figure 1.** Cu azide model system used in section II. Note that the same coordinate system applies to the $d_{xy}$ orbitals on both coppers.

**Scheme I**

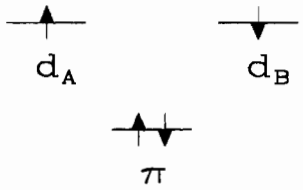


properties considered in this study to the ground-state properties of bridged dimers are discussed.

## II. Theoretical Framework

In this section, the ground and charge-transfer (CT) excited-state energies of bridged transition metal dimers are derived. The treatment focuses specifically on the $(\pi^{nb})_\sigma \rightarrow$ Cu CT transition of a cis $\mu$-1,3 azide bridged Cu(II) dimer. In part A, the diagonal CT state splittings are determined and it is shown that the splitting parameters are identical to those of exciton theory. Hence, this description is called the "excitonic model". As the coupling of transition dipole vectors (transition dipole vector coupling, TDVC) accounts for the major part of the electronic CT state splitting, the excitonic model basically coincides with the TDVC model which has been used earlier to interpret CT spectra of bridged dimers.[10,15] The excitonic model may be formulated using either atomic metal orbitals (VB formalism) or using delocalized molecular orbital (MO) metal basis functions (MO formalism). In part B, the bonding of metal and ligand orbitals is considered explicitly and a method for the theoretical calculation of CT state splittings is developed. Within the VB formalism, configuration interaction (CI) between the VB *states* of part A is introduced (VBCI model, part B.1). In the MO formalism, the metal type MO's of part A are mixed with ligand orbitals and states are built from the admixed *orbitals* (MO model, part B.2). Both descriptions are shown to agree in the description of triplet states which provides a method to calculate VBCI parameters by molecular orbital transition state calculations.

**II.A. Excitonic Model.** The structurally characterized cis $\mu$-1,3 azide bridged Cu(II) dimer, [Cu(L–Et)$N_3$], is idealized as depicted in Figure 1. The coordinate system is chosen such that the unpaired electron on each Cu(II), $Cu_A$ and $Cu_B$, is located in the $d_{xy}$ orbital. The phases of both Cu d orbitals, $d_A$ and $d_B$, are set to obtain positive overlap with the doubly occupied bridging in-plane $(\pi^{nb})_\sigma$ orbital of azide. This three-orbital system contains four electrons and is the binding framework of the dimeric complex.

In order to simplify the treatment, the $(\pi^{nb})_\sigma$ orbital of azide is orthogonalized to the metal orbitals

$$\pi \equiv (1/\sqrt{1-S_{d\pi}^2})((\pi^{nb})_\sigma - S_{d\pi}(d_A + d_B)) \qquad (1)$$

with the overlap integral $S_{d\pi} \equiv \langle d_A|(\pi^{nb})_\sigma\rangle = \langle d_B|(\pi^{nb})_\sigma\rangle$. For simplicity, it is also assumed that the metal orbitals do not overlap, $\langle d_A|d_B\rangle = 0$. Thus, $\langle d_A|\pi\rangle = \langle d_B|\pi\rangle = 0$. In the ground state of the dimer, each Cu is occupied by one electron in $d_A$ and $d_B$ with two paired electrons in $\pi$ (Scheme I). The two unpaired electrons couple to form singlet and triplet states. The corresponding wave functions ${}^i\Psi_j^{GS}$, $i = 1, 3$ and $j = +, -$, are compiled in Table I (see "valence bond" column).

An azide $\rightarrow$ Cu CT transition corresponds to a shift of an electron from $\pi$ to $d_A$ resulting in a $Cu^+(d^{10})$ ion on site A (Scheme II). Alternatively, the electron may be shifted from $\pi$ to $d_B$ forming a reduced Cu on site B. The corresponding singlet wave functions ${}^1\Phi_A{}^{CT}$ and ${}^1\Phi_B{}^{CT}$ are given in Table I. Proper dimer eigenstates ${}^1\Psi_+{}^{CT}$ and ${}^1\Psi_-{}^{CT}$ are linear combinations of ${}^1\Phi_A{}^{CT}$ and ${}^1\Phi_B{}^{CT}$; analogous considerations apply for the triplet CT states (cf. Table I).

Instead of starting from the atomic orbitals $d_A$ and $d_B$, one can equally use the molecular orbitals (MO's)

$$d_- = (1/\sqrt{2})(d_A + d_B) \qquad (2a)$$

$$d_+ = (1/\sqrt{2})(d_A - d_B) \qquad (2b)$$

along with the azide $\pi$ orbital. It will be shown in part II.B that $d_-$ is raised in energy due to a bonding interaction with $\pi$. At the present level, however, $d_-$ and $d_+$ are only separated by

$$\langle d_-\rangle - \langle d_+\rangle = 2\langle d_A|h(1)|d_B\rangle \equiv 2h_{AB} \qquad (3)$$

which is assumed to be very small as $d_A$ and $d_B$ are far apart and do not overlap. The four-electron ground and CT excited wave functions arising from $\pi$, $d_+$, and $d_-$, are compiled in Table I, right. $h(1)$ in (3) denotes the one-electron part of the Hamiltonian $H$ of the four-electron dimer system given by

$$H = \sum_{i=1,4} h(i) + \sum_{\substack{i,j=1,4 \\ i<j}} e^2/r_{ij} \qquad (4)$$

Evaluation of the diagonal energies of $H$ with the VB or MO CT state functions of Table I leads to the following CT state energies:

$$\langle {}^1\Psi_+{}^{CT}\rangle = \overline{\Delta E} + J_{d\pi} + 2I - L - h_{AB} \qquad (5a)$$

$$\langle {}^1\Psi_-{}^{CT}\rangle = \overline{\Delta E} + J_{d\pi} - 2I + L + h_{AB} \qquad (5b)$$

$$\langle {}^3\Psi_+{}^{CT}\rangle = \overline{\Delta E} - J_{d\pi} - L - h_{AB} \qquad (5c)$$

$$\langle {}^3\Psi_-{}^{CT}\rangle = \overline{\Delta E} - J_{d\pi} + L + h_{AB} \qquad (5d)$$

with

$$L = \langle d_A\pi|e^2/r_{12}|d_B\pi\rangle = \int d_A{}^*(1)\,\pi^*(2)\,e^2/r_{12}\,d_B(1)\pi(2)\,d\tau \qquad (6a)$$

$$I = \langle d_A\pi|e^2/r_{12}|\pi d_B\rangle \qquad (6b)$$

$$N = \langle d_A d_B|e^2/r_{12}|d_A d_A\rangle = \langle d_A d_B|e^2/r_{12}|d_B d_B\rangle \qquad (6c)$$

$$J_{d\pi} = \langle d_A\pi|e^2/r_{12}|\pi d_A\rangle = \langle d_B\pi|e^2/r_{12}|\pi d_B\rangle \qquad (6d)$$

$\Delta E$ is an average CT energy given by the energy difference

$$\overline{\Delta E} = (1/4)(\langle {}^1\Psi_+{}^{CT}\rangle + \langle {}^1\Psi_-{}^{CT}\rangle + \langle {}^3\Psi_+{}^{CT}\rangle + \langle {}^3\Psi_-{}^{CT}\rangle) - (1/2)(\langle {}^1\Psi_+{}^{GS}\rangle + \langle {}^3\Psi_-{}^{GS}\rangle) = K_{d_A d_A} - K_{\pi\pi} + J_{d\pi} - K_{d\pi} + K_{d_A d_B} - J_{dd} + \langle d_A\rangle - \langle \pi\rangle \qquad (7)$$

**Table I.** Wave Functions

| wave function | valence bond | molecular orbital |
|---|---|---|
| Ground State | | |
| $^1\Psi_+^{G.S.}$ | $= \frac{1}{\sqrt{2}}\left(\lvert d_A^2 \bar{\pi}\pi d_B^2\rvert - \lvert d_A^2 \pi\bar{\pi} d_B^2\rvert\right)$ | $= \frac{1}{\sqrt{2}}\left(\lvert d^2\bar{\pi}\pi\rvert - \lvert d^2\pi\bar{\pi}\rvert\right)$ |
| | | $= \frac{1}{\sqrt{2}}(^1\Phi_+^{G.S.} - {}^1\Phi_+^{CT})$ |
| $^3\Psi_-^{G.S.}(M_s=+1)$ | $= \lvert d_A^2 \bar{\pi}\pi d_B^+\rvert$ | $= -\lvert d^2\bar{\pi}\pi\rvert$ |
| $^3\Psi_-^{G.S.}(M_s=0)$ | $= \frac{1}{\sqrt{2}}\left(\lvert d_A^2 \bar{\pi}\pi d_B^-\rvert + \lvert d_A^+ \bar{\pi}\pi d_B^+\rvert\right)$ | $= -\frac{1}{\sqrt{2}}\left(\lvert d^2\bar{\pi}\pi\rvert + \lvert d^+\bar{\pi}\pi\rvert\right)$ |
| $^3\Psi_-^{G.S.}(M_s=-1)$ | $= \lvert d_A^+ \bar{\pi}\pi d_B^-\rvert$ | $= -\lvert d^+\bar{\pi}\pi\rvert$ |
| Charge Transfer State | | |
| $^1\Phi_A^{CT}$ | $= \frac{1}{\sqrt{2}}\left(\lvert d_A^2 d_A^- \bar{\pi} d_B^+\rvert - \lvert d_A^2 d_A^+ \bar{\pi} d_B^-\rvert\right)$ | |
| $^1\Phi_B^{CT}$ | $= \frac{1}{\sqrt{2}}\left(\lvert d_B^2 d_B^- \bar{\pi} d_A^+\rvert - \lvert d_B^2 d_B^+ \bar{\pi} d_A^-\rvert\right)$ | |
| $^1\Psi_+^{CT}$ | $= \frac{1}{\sqrt{2}}(^1\Phi_A^{CT} + {}^1\Phi_B^{CT})$ | $= \frac{1}{\sqrt{2}}\left(\lvert d^2 d^-\bar{\pi} d^+\rvert - \lvert d^2 d^+\bar{\pi} d^-\rvert\right)$ |
| $^1\Psi_-^{CT}$ | $= \frac{1}{\sqrt{2}}(^1\Phi_A^{CT} - {}^1\Phi_B^{CT})$ | $= \frac{1}{\sqrt{2}}\left(\lvert d^2 d^-\bar{\pi} d^+\rvert - \lvert d^2 d^+\bar{\pi} d^-\rvert\right)$ |
| $^3\Phi_A^{CT}(M_s=+1)$ | $= \lvert d_A^2 d_A^- \bar{\pi} d_B^+\rvert$ | |
| $^3\Phi_A^{CT}(M_s=0)$ | $= \frac{1}{\sqrt{2}}\left(\lvert d_A^2 d_A^- \bar{\pi} d_B^-\rvert + \lvert d_A^2 d_A^+ \bar{\pi} d_B^+\rvert\right)$ | |
| $^3\Phi_A^{CT}(M_s=-1)$ | $= \lvert d_A^2 d_A^+ \bar{\pi} d_B^-\rvert$ | |
| $^3\Phi_B^{CT}(M_s=+1)$ | $= \lvert d_B^2 d_B^- \bar{\pi} d_A^+\rvert$ | |
| $^3\Phi_B^{CT}(M_s=0)$ | $= \frac{1}{\sqrt{2}}\left(\lvert d_B^2 d_B^- \bar{\pi} d_A^-\rvert + \lvert d_B^2 d_B^+ \bar{\pi} d_A^+\rvert\right)$ | |
| $^3\Phi_B^{CT}(M_s=-1)$ | $= \lvert d_B^2 d_B^+ \bar{\pi} d_A^-\rvert$ | |
| $^3\Psi_+^{CT}(M_s=+1)$ | $= \frac{1}{\sqrt{2}}\left({}^3\Phi_A^{CT}(M_s=+1) + {}^3\Phi_B^{CT}(M_s=+1)\right)$ | $= \lvert d^2 d^-\bar{\pi} d^+\rvert$ |
| $^3\Psi_+^{CT}(M_s=0)$ | $= \frac{1}{\sqrt{2}}\left({}^3\Phi_A^{CT}(M_s=0) + {}^3\Phi_B^{CT}(M_s=0)\right)$ | $= \frac{1}{\sqrt{2}}\left(\lvert d^2 d^-\bar{\pi} d^-\rvert + \lvert d^2 d^+\bar{\pi} d^+\rvert\right)$ |
| $^3\Psi_+^{CT}(M_s=-1)$ | $= \frac{1}{\sqrt{2}}\left({}^3\Phi_A^{CT}(M_s=-1) + {}^3\Phi_B^{CT}(M_s=-1)\right)$ | $= \lvert d^2 d^+\bar{\pi} d^-\rvert$ |
| $^3\Psi_-^{CT}(M_s=+1)$ | $= \frac{1}{\sqrt{2}}\left({}^3\Phi_A^{CT}(M_s=+1) - {}^3\Phi_B^{CT}(M_s=+1)\right)$ | $= \lvert d^2 d^+\bar{\pi} d^-\rvert$ |
| $^3\Psi_-^{CT}(M_s=0)$ | $= \frac{1}{\sqrt{2}}\left({}^3\Phi_A^{CT}(M_s=0) - {}^3\Phi_B^{CT}(M_s=0)\right)$ | $= \frac{1}{\sqrt{2}}\left(\lvert d^2 d^-\bar{\pi} d^-\rvert + \lvert d^2 d^+\bar{\pi} d^+\rvert\right)$ |
| $^3\Psi_-^{CT}(M_s=-1)$ | $= \frac{1}{\sqrt{2}}\left({}^3\Phi_A^{CT}(M_s=-1) - {}^3\Phi_B^{CT}(M_s=-1)\right)$ | $= \lvert d^2 d^-\bar{\pi} d^+\rvert$ |
| Metal-to-Metal-CT | | |
| $^1\Psi_+^{MMCT}$ | $= \frac{1}{\sqrt{2}}\left(\lvert d_A^2 d_A^- \bar{\pi}\pi\rvert + \lvert d_B^2 d_B^- \bar{\pi}\pi\rvert\right)$ | $= \frac{1}{\sqrt{2}}\left(\lvert d^2 d^-\bar{\pi}\pi\rvert + \lvert d^2 d^-\bar{\pi}\pi\rvert\right)$ |
| | | $= \frac{1}{\sqrt{2}}(^1\Phi_+^{G.S.} + {}^1\Phi_+^{CT})$ |
| $^1\Psi_-^{MMCT}$ | $= \frac{1}{\sqrt{2}}\left(\lvert d_A^2 d_A^- \bar{\pi}\pi\rvert - \lvert d_B^2 d_B^- \bar{\pi}\pi\rvert\right)$ | $= \frac{1}{\sqrt{2}}\left(\lvert d^2 d^-\bar{\pi}\pi\rvert - \lvert d^2 d^-\bar{\pi}\pi\rvert\right)$ |
| Double Charge Transfer | | |
| $^1\Psi_+^{DCT}$ | $= \lvert d_A^2 d_A^- d_B^2 d_B^-\rvert$ | $= \lvert d^2 d^-\bar{\pi}^2 d^-\rvert$ |

where the Coulomb, exchange, and one-electron integrals, respectively, are given by

$$K_{ij} = \langle ij|e^2/r_{12}|ij\rangle \qquad J_{ij} = \langle ij|e^2/r_{12}|ji\rangle \tag{8}$$

$$\langle d_A\rangle = \langle d_A|h(1)|d_A\rangle \qquad \langle \pi\rangle = \langle \pi|h(1)|\pi\rangle \tag{9}$$

In the following, it is assumed that $K_{d_Ad_B} \approx J_{dd} \approx 0$. For further insight into eq 7, the "monomer CT transition"[25] is considered.

**Scheme II**

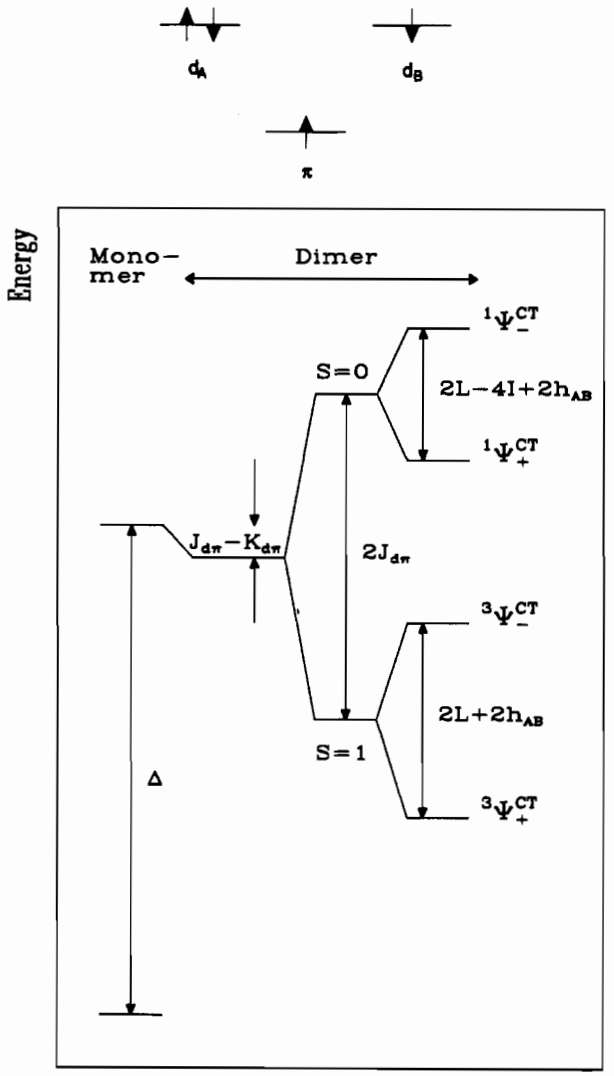


**Figure 2.** Excitonic splitting scheme of each monomer CT state in a dimer.

The ground and CT excited states are in this case given by the three-electron functions

$$\Psi_{GS} = |d_A^+\pi^+\pi^-| \qquad \Psi_{CT} = |d_A^+ d_A^-\pi^+| \tag{10}$$

and the CT transition energy results as

$$\Delta \equiv \langle\Psi_{CT}\rangle - \langle\Psi_{GS}\rangle = K_{d_Ad_A} - K_{\pi\pi} + \langle d_A\rangle - \langle\pi\rangle \tag{11}$$

Therefore,

$$\overline{\Delta E} = \Delta + J_{d\pi} - K_{d\pi} \tag{12}$$

and the overall shift of the dimer with respect to the monomer CT transition is given by $J_{d\pi} - K_{d\pi}$ (see Figure 2). From (5), the following CT splittings are obtained (see Figure 2):

$$\langle {}^1\Psi_-{}^{CT}\rangle - \langle {}^1\Psi_+{}^{CT}\rangle = 2L - 4I + 4N + 2H_{AB} \tag{13a}$$

$$\langle {}^3\Psi_-{}^{CT}\rangle - \langle {}^3\Psi_+{}^{CT}\rangle = 2L + 4N + 2H_{AB} \tag{13b}$$

The CT singlet states are split symmetrically by three two-electron parameters, $L$, $I$, and $N$, and the CT triplet states are split symmetrically only by $L$ and $N$. Apart from $h_{AB}$, which is

(25) Strictly speaking, the $\pi$ orbital in (10) is not the proper monomer ligand orbital due to (1). Hence, $\Delta$ in (11) may not be considered as the monomer CT energy but as the CT energy of a monomer subunit (e.g. A) of the dimer where all coupling to the unpaired electron on $Cu_B$ has been neglected.

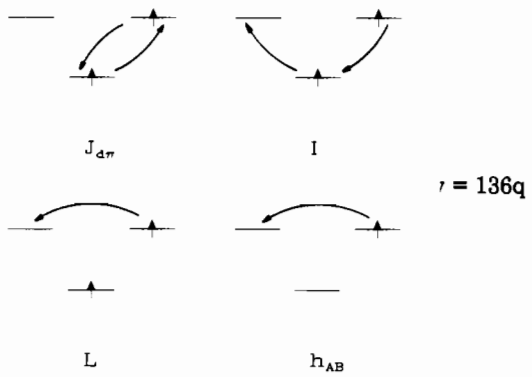


**Figure 3.** Pictorial representation of the two-electron integrals $I$, $J_{d\pi}$, and $L$ and the one-electron integral $h_{AB}$.

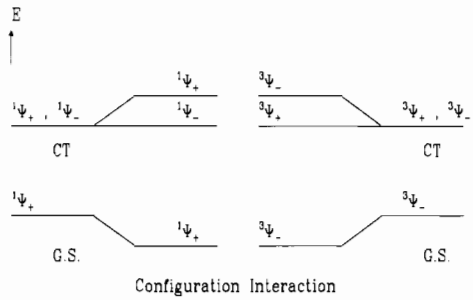


**Figure 4.** Singlet and triplet states of a Cu(II) dimer with configuration interaction.

small, the above result (eqs 13a,b) is identical to the excitonic splitting scheme as derived by El Sayed and Robinson.[26] The difference between the mean singlet and the mean triplet energies, i.e. the CT singlet–triplet gap, is given by

$$(1/2)[(\langle {}^1\Psi_+{}^{CT}\rangle + \langle {}^1\Psi_-{}^{CT}\rangle) - (\langle {}^3\Psi_+{}^{CT}\rangle + \langle {}^3\Psi_-{}^{CT}\rangle)] = 2J_{d\pi} \quad (14)$$

This excited state magnetic coupling constant $J_{d\pi}$ (eq 6d) has to be distinguished from the ground-state magnetic coupling constant $J_{dd}$ given by

$$\langle {}^3\Psi_-{}^{GS}\rangle - \langle {}^1\Psi_+{}^{GS}\rangle = -2J_{dd} = -2\langle d_A d_B|e^2/r_{12}|d_B d_A\rangle \quad (15)$$

In total, the splitting of the CT states (eqs 13 and 14) can be expressed in terms of four parameters, $I$, $J_{d\pi}$, $L$, and $N$. $I$ represents an interaction between two exchange charge densities, $d_A{}^*(1)\pi(1)$ and $\pi^*(2)d_B(2)$, and has been termed Coulomb mediated excitation transfer (see Figure 3).[22] Clasically, $4I$ may be viewed as interaction energy between two transition dipoles.[23a] $L$, the exchange mediated excitation transfer,[23b] represents the interaction between the exchange charge density $d_A{}^*(1)d_B(1)$ and the charge density on the bridge, $\pi^*(2)\pi(2)$ (see Figure 3). Similarly, $N$ represents the interaction of $d_A{}^*d_B$ with $d_A{}^*d_A$. As the exchange charge density for $Cu_A$ and $Cu_B$ will be highest between the two atoms, i.e. on the bridge, $N$ can be assumed to be small as compared to $L$ and is therefore neglected. Finally, the excited-state exchange integral $J_{d\pi}$ is the self-interaction of the metal–ligand exchange charge density (see Figure 3), just as the ground-state exchange integral $J_{dd}$ is the self-interaction of the metal–metal exchange charge density.

So far, ligand orbitals orthogonalized to metal d functions have been used in the many-electron dimer wave functions. This way, the one-electron contribution $2H_{AB}$ to the excited CT state splitting is negligible and only the two-electron integrals $L$ and $I$ account for the dimer splitting. In the case of the azide-bridged dimer $[Cu_2(L\text{–}Et)(N_3)]$, the $4I$ contribution to the CT state splitting has been estimated with the TDVC model to 275 $cm^{-1}$.

(26) El Sayed, M. A.; Robinson, G. W. *Mol. Phys.* **1961**, *4*, 273–286.

**Scheme III**

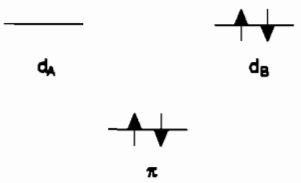


On the other hand, a splitting of $\langle {}^1\Psi_+{}^{CT}\rangle - \langle {}^1\Psi_-{}^{CT}\rangle$ of 3600 $cm^{-1}$ has been observed experimentally.[15] As it is known from exciton theory that the two-electron $L$ integral is even smaller than $I$,[23b,26] this level of description is clearly insufficient to describe the CT splitting. In addition, the excitonic model is not able to explain excited-state antiferromagnetism as the exchange integral $J_{d\pi}$ is positive and the CT triplets lie below the CT singlets (Figure 2). Hence, off-diagonal terms are considered in the following sections.

**II.B.1. Valence-Bond CI Model.** In terms of the valence-bond (VB) formalism, bonding is introduced as a configuration interaction (CI). First, the ground and CT state triplets are considered. The off-diagonal matrix element between these states is

$$\langle {}^3\Psi_-{}^{GS}|H|{}^3\Psi_-{}^{CT}\rangle = \sqrt{2}\langle d_A|h(1)|\pi\rangle \equiv \sqrt{2}h_{d_A\pi} \equiv h_{d\pi} \quad (16)$$

This transfer integral corresponds to a one-electron jump from the bridging ligand to the metal, i.e. a CT transition. The secular determinant

$$\begin{vmatrix} \langle {}^3\Psi_-{}^{GS}\rangle - E & h_{d\pi} \\ h_{d\pi} & \langle {}^3\Psi_-{}^{CT}\rangle - E \end{vmatrix} = 0 \quad (17)$$

describes the mutual repulsion between the triplet ground and the "–" CT excited state. ${}^3\Psi_+{}^{CT}$ cannot interact with the triplet ground state, $\langle {}^3\Psi_-{}^{GS}|H|{}^3\Psi_+{}^{CT}\rangle = 0$. Hence, the interaction (16) splits the "+" and "–" CT triplets which are thus far degenerate (except in section II.A where the two-electron integral $L$ and $h_{AB}$ were included). The admixed triplet functions are

$$({}^3\Psi_-{}^{CT})' = \sqrt{1-\lambda^2}\ {}^3\Psi_-{}^{CT} - \lambda\ {}^3\Psi_-{}^{GS} \quad (18a)$$

$$({}^3\Psi_+{}^{CT})' = {}^3\Psi_+{}^{CT} \quad (18b)$$

$$({}^3\Psi_-{}^{GS})' = \sqrt{1-\lambda^2}\ {}^3\Psi_-{}^{GS} + \lambda\ {}^3\Psi_-{}^{CT} \quad (18c)$$

and, for $|h_{d\pi}/\Delta| \ll 1$, the triplet CT splitting is given by

$$\langle ({}^3\Psi_-{}^{CT})'\rangle - \langle {}^3\Psi_+{}^{CT}\rangle = h_{d\pi}{}^2/\Delta \quad (19)$$

Analogous considerations apply for the ground and CT state singlets. In contrast to the triplets, the "+" components interact

$$\langle {}^1\Psi_+{}^{GS}|H|{}^1\Psi_+{}^{CT}\rangle = h_{d\pi} \quad (20)$$

which causes a singlet CT state splitting opposite to the triplet splitting:

$$\langle ({}^1\Psi_+{}^{CT})'\rangle - \langle {}^1\Psi_-{}^{CT}\rangle = h_{d\pi}{}^2/\Delta \quad (21)$$

($|h_{d\pi}/\Delta| \ll 1$) (Figure 4). However, the CT excited singlets are not only interacting with the singlet ground state. Starting from the CT excited configuration, two more singlet states can be reached by one-electron transitions: the unpaired electron on one copper may jump to the bridge, corresponding to a transition to a metal → metal CT (MMCT) state (Scheme III) or the unpaired electron on the bridge may jump to the copper containing one hole corresponding to a second CT transition (double CT state, DCT) (Scheme IV). The corresponding MMCT and DCT wave functions are compiled in Table I. After determination of the relevant off-diagonal elements, the full singlet "+" state secular

**Scheme IV**

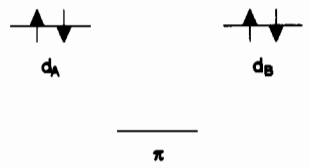


determinant is given by

$$\begin{vmatrix} \langle {}^1\Psi_+{}^{GS}\rangle - E & h_{d\pi} & 0 & 0 \\ h_{d\pi} & \langle {}^1\Psi_+{}^{CT}\rangle - E & h_{d\pi} & \sqrt{2}h_{d\pi} \\ 0 & h_{d\pi} & \langle {}^1\Psi_+{}^{MMCT}\rangle - E & 0 \\ 0 & \sqrt{2}h_{d\pi} & 0 & \langle {}^1\Psi_+{}^{DCT}\rangle - E \end{vmatrix} = 0 \quad (22)$$

and the "–" singlet secular determinant by

$$\begin{vmatrix} \langle {}^1\Psi_-{}^{CT}\rangle - E & h_{d\pi} \\ h_{d\pi} & \langle {}^1\Psi_-{}^{MMCT}\rangle - E \end{vmatrix} = 0 \quad (23)$$

Note that, for the triplets, no MMCT or DCT states are possible. Neglecting two-electron integrals, the secular determinants (17), (22), and (23) involve four parameters: the mean CT energy $\overline{\Delta E} \approx \Delta$ (cf. (11), (12)), the transfer integral $h_{d\pi}$, the energy of the MMCT state $E_{MMCT}$, and the energy of the DCT state $E_{DCT}$. The secular problems are solved algebraically in section III.B for the cis $\mu$-1,3 azide dimer. If $\Delta < E_{MMCT} < E_{DCT}$, both ${}^1\Psi_+{}^{CT}$ and ${}^1\Psi_-{}^{CT}$ are shifted to lower energy by interaction with the MMCT states of equal symmetry. As the triplet CT states are not subject to such interaction, the CT singlets lie below the triplets corresponding to an *excited-state antiferromagnetism* (ESAF). Finally, the singlet ground state ${}^1\Psi_+{}^{GS}$ is shifted below the triplet ground state ${}^3\Psi_-{}^{GS}$ (ground-state antiferromagnetism, GSAF) as it interacts with a singlet CT state lowered by ESAF below the triplet CT state.

**II.B.2. Molecular Orbital Model.** In section II.A, the molecular orbital description of a bridged dimer has been introduced by combining the copper atomic orbitals $d_A$ and $d_B$ into the MO basis functions $d_+$ and $d_-$ (eq 21) which have been treated as quasi degenerate. Now, metal–ligand bonding is introduced by mixing $d_-$ with $\pi$:

$$\pi' = \sqrt{1-\lambda^2}\pi + \lambda d_- \quad (24a)$$

$$d_-' = \sqrt{1-\lambda^2}d_- - \lambda\pi \quad (24b)$$

$$d_+' = d_+ \quad (24c)$$

The mixing coefficient $\lambda$ and the interaction energy are determined from the secular determinant

$$\begin{vmatrix} \langle\pi\rangle - E & h_{d\pi} \\ h_{d\pi} & \langle d_-\rangle - E \end{vmatrix} = 0 \quad (25)$$

with

$$h_{d\pi} = \langle d_-|h(1)|\pi\rangle \quad (26)$$

(cf. (16)). (25) describes a repulsion between $\pi$ and $d_-$. As $\langle d_+|h|\pi\rangle = 0$, $d_+$ and $d_-'$ are split with $d_-'$ being higher in energy (HOMO–LUMO splitting):

$$\langle d_-'\rangle - \langle d_+\rangle = \Delta E_{HL} \quad (27)$$

With $\langle d_-\rangle - \langle\pi\rangle \approx \Delta$ and $|h_{d\pi}/\Delta| \ll 1$

$$\Delta E_{HL} \approx \frac{(h_{d\pi})^2}{\Delta} \quad (28)$$

The MO singlet ground state configuration (cf. Table I) is given by Scheme V, and the two singlet CT states ${}^1\Psi_+{}^{CT}$ and ${}^1\Psi_-{}^{CT}$ are given by Scheme VI. Correspondingly, the triplet $M_S = +1$ ground state is represented by Scheme VII, and the two triplet CT states

**Scheme V**

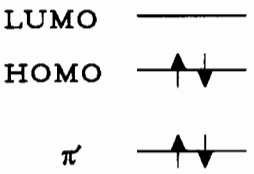


**Scheme VI**

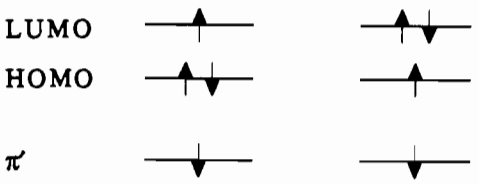


**Scheme VII**

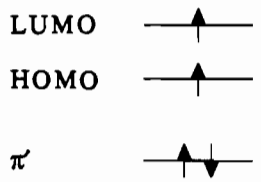


**Scheme VIII**

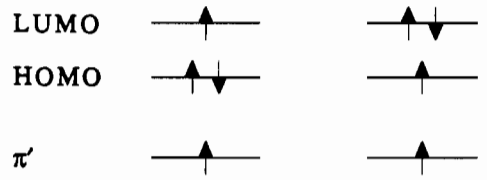


${}^3\Psi_+{}^{CT}$ and ${}^3\Psi_-{}^{CT}$ are given by Scheme VIII. From Schemes VI and VIII and neglecting two-electron integrals, the singlet and triplet CT splittings are given by the orbital difference

$$(\langle {}^i\Psi_-\rangle - \langle {}^i\Psi_+\rangle)_{MO}^{\text{one-electron}} = \langle d_-'\rangle - \langle d_+\rangle = \Delta E_{HL} \qquad i = 1, 3 \quad (29)$$

This result may also be obtained using the MO singlet and triplet CT functions of Table I but with the admixed orbitals of (24) instead of (2). Note that with $\Delta E_{HL} = h_{d\pi}{}^2/\Delta$ (eq 28) the MO splitting (eq 29) is identical with the VB splitting (eq 19) for the CT triplets but opposite to the VB splitting (eq 21) for the CT singlets. In fact, both models (MO and VBCI) coincide for the triplets, which can be shown by expanding the MO triplet CT functions of Table I containing the admixed orbitals of (24) into those containing the unperturbed orbitals of (2); this way, the VBCI wave functions of (18) are obtained. The same correspondence between MO and VBCI holds for the ground-state triplets. Hence, it is possible to calculate the VBCI parameters $\Delta$ and $h_{d\pi}$ by MO methods (see sections III.A.e and III.B).

The singlet CT excited-state splitting (eq 29) predicted by the MO model ("–" higher than "+") is opposite to the ordering given by the VBCI model ("+" higher than "–"; cf. section II.A, (21)). The reason for this contradiction is a different contribution of the MMCT in the CT state which is seen by again expanding the MO many-electron wave functions containing the mixed orbitals $\pi'$ and $d_-'$ into those containing the unperturbed orbitals $\pi$ and $d_-$. Of course, CI could also be employed in the MO framework, which would remove the disagreement with the VBCI prediction.

So far, the $(\pi^{nb})_v \rightarrow$ Cu CT transition has not been considered. The azide $(\pi^{nb})_v$ orbital is oriented vertical to the Cu–$N_2$–Cu plane and has a comparatively weak $\pi$-interaction with the metal. It is therefore at higher energy than the in-plane orbital $(\pi^{nb})_\sigma$. In addition, the overlap between $(\pi^{nb})_v$ and the singly occupied,

highest metal orbital is small. Hence, the $(\pi^{nb})_v \rightarrow$ Cu CT transition is at lower energy than the $(\pi^{nb})_\sigma$ CT transition and has a much smaller intensity. In analogy to the $(\pi^{nb})_\sigma$ CT state, the $(\pi^{nb})_v$ CT state is doubly degenerate and may split by electronic interactions. This point is further considered in section III.B.

To summarize, the treatment of section II.B has shown the following: (i) The VBCI model allows a qualitative understanding of the effects of CT state splitting and CT state antiferromagnetism. (ii) The MO model provides a physical picture for the VBCI parameters $\Delta$ and $h_{d\pi}$ which determine the CT state energies. In particular, the triplet CT splitting is given by the HOMO–LUMO splitting. As the triplet CT state descriptions coincide in the MO and VBCI model, $\Delta$ and $h_{d\pi}$ are accessible from a MO calculation (see the following section).

## III. Application to Copper Azide Model Systems: Ground- and Excited-State Properties

**III.A. Molecular Orbital Model. III.A.1. Computational Methods.** The electronic structure of a copper(II)–azide monomer and a cis $\mu$-1,3 dimer was calculated using the standard version of the SCF–X$\alpha$–SW method. Both mono- and binuclear copper azide systems exist which have been structurally characterized and studied spectroscopically.[15,16] The geometry used for the monomer calculation was adapted from that of the $[(L'–O)Cu(N_3)]\cdot H_2O$ complex,[27] which is an almost ideal square-based pyramid with two nitrogen coordinating ligands, one phenoxo group, and one azide in the basal plane. This coordination was simplified in the calculation to square planar by placing three ammonia ligands and the azide in the basal plane, resulting in $C_s$ molecular symmetry. The dimer calculation is based on the $[Cu_2(L–Et)(N_3)]^{2+}$ ion, where the coordination around each Cu center is also close to square-pyramidal.[16] The basal Cu coordination of two benzimidazolyl nitrogens, bridging alkoxy (approximated as hydroxide), and azide was also idealized to square planar, resulting in $C_{2v}$ molecular symmetry. The input geometries of monomer and dimer are compiled in Table II.

Spin-unrestricted SCF–X$\alpha$–SW calculations[28] were performed on the monomer and the dimer. In addition, broken symmetry SCF–X$\alpha$–SW calculations were performed on the dimer according to the procedure of Noodleman.[29] Both systems were placed in Watson spheres in order to ensure overall neutrality. The calculations were considered to be converged when the largest relative change in the potential between subsequent iterations was less than $1 \times 10^{-5}$. $\alpha$ values for the atomic regions were taken from the table of Schwarz,[30] and those in the inter- and outer-sphere regions were weighted averages of the atomic $\alpha$ values based on the number of valence electrons in the neutral free atoms. All calculations were performed with Cu, O, ammonia–N, and H sphere radii fixed at 2.95, 1.84, 1.70, and 1.17 bohr, respectively. These values have been optimized in a previous X$\alpha$ study of copper peroxide systems;[21] in particular, the $O_2^{2-}$ $\pi^*_\sigma \rightarrow$ Cu charge-transfer transition energy was reproduced for a copper peroxide monomer which corresponds to the azide monomer system studied here. The azide sphere radii were determined in a calculation of free azide ($N_3^-$) with an equilibrium N–N bond distance of 2.2200 bohr placed in a Watson sphere of +1 charge. The photoelectron spectrum of azide and the transition energy to the lowest excited state were reproduced satisfactorily with radii of 1.6 bohr (terminal N) and 1.4 bohr (central N).[31]

**Table II.** Input Geometries of Copper Azides[a]

| no. | atom | position $x$ | position $y$ | position $z$ | radius | $\alpha$ |
|---|---|---|---|---|---|---|
| | | (A) Azide Monomer | | | | |
| 1 | out | −0.1102 | −0.9273 | 0.0000 | 8.8371 | 0.78276 |
| 2 | Cu | 0.2070 | −0.9527 | 0.0000 | 2.9500 | 0.70697 |
| 3 | N4 | 1.3460 | 2.6590 | 0.0000 | 1.6000 | 0.75197 |
| 4 | N5 | −0.1821 | 4.3827 | 0.0000 | 1.3000 | 0.75197 |
| 5 | N6 | −1.5445 | 6.2682 | 0.0000 | 1.6000 | 0.75197 |
| 6 | N3 | 3.9548 | −1.4414 | 0.0000 | 1.7000 | 0.75197 |
| 7 | N1 | −0.7215 | −4.8635 | 0.0000 | 1.7000 | 0.75197 |
| 8 | N2 | −3.5246 | −0.0861 | 0.0000 | 1.7000 | 0.75197 |
| 9 | H1A | −2.6003 | −5.0651 | 0.0000 | 1.1700 | 0.97804 |
| 10 | H1B | 0.0000 | −5.6822 | −1.5429 | 1.1700 | 0.97804 |
| 11 | H2A | −3.7348 | 1.7921 | 0.0000 | 1.1700 | 0.97804 |
| 12 | H2B | −4.3507 | −0.7983 | −1.5429 | 1.1700 | 0.97804 |
| 13 | H3A | 4.3493 | −3.2896 | 0.0000 | 1.1700 | 0.97804 |
| 14 | H3B | 4.6941 | −0.6397 | −1.5429 | 1.1700 | 0.97804 |
| 15 | H1B | 0.0000 | −5.6822 | 1.5429 | 1.1700 | 0.97804 |
| 16 | H2B | −4.3507 | −0.7983 | 1.5429 | 1.1700 | 0.97804 |
| 17 | H3B | 4.6941 | −0.6397 | 1.5429 | 1.1700 | 0.97804 |
| | | (B) Azide Dimer | | | | |
| 1 | out | 0.0000 | 0.0012 | 0.0000 | 9.1336 | 0.77702 |
| 2 | Cu1 | −3.4157 | 0.0012 | 0.0000 | 2.9500 | 0.70697 |
| 3 | Cu2 | 3.4157 | 0.0012 | 0.0000 | 2.9500 | 0.70697 |
| 4 | N5 | −2.1730 | 3.6395 | 0.0000 | 1.6000 | 0.75197 |
| 5 | N6 | 0.0000 | 3.7344 | 0.0000 | 1.3000 | 0.75197 |
| 6 | N7 | 2.1730 | 3.6395 | 0.0000 | 1.6000 | 0.75197 |
| 7 | O–H | 0.0000 | −1.3511 | 0.0000 | 1.8400 | 0.74447 |
| 8 | H–O | 0.0000 | −3.2408 | 0.0000 | 1.1700 | 0.97804 |
| 9 | N1 | −7.1294 | 0.7029 | 0.0000 | 1.7000 | 0.75197 |
| 10 | N2 | −4.5798 | −3.7134 | 0.0000 | 1.1700 | 0.75197 |
| 11 | N3 | 7.1294 | 0.7029 | 0.0000 | 1.7000 | 0.75197 |
| 12 | N4 | 4.5798 | −3.7134 | 0.0000 | 1.7000 | 0.75197 |
| 13 | H1A | −7.4185 | 2.5703 | 0.0000 | 1.1700 | 0.97804 |
| 14 | H1B | −7.9145 | −0.0555 | −1.5426 | 1.1700 | 0.97804 |
| 15 | H2A | −3.0685 | −4.8480 | 0.0000 | 1.1700 | 0.97804 |
| 16 | H2B | −5.6182 | −4.0489 | −1.5426 | 1.1700 | 0.97804 |
| 17 | H3A | 7.4185 | 2.5703 | 0.0000 | 1.1700 | 0.97804 |
| 18 | H3B | 7.9145 | −0.0555 | −1.5426 | 1.1700 | 0.97804 |
| 19 | H4A | 3.0685 | −4.8480 | 0.0000 | 1.1700 | 0.97804 |
| 20 | H4B | 5.6182 | −4.0489 | −1.5426 | 1.1700 | 0.97804 |
| 21 | H1B | −7.9145 | −0.0555 | 1.5426 | 1.1700 | 0.97804 |
| 22 | H2B | −5.6182 | −4.0489 | 1.5426 | 1.1700 | 0.97804 |
| 23 | H3B | 7.9145 | −0.0555 | 1.5426 | 1.1700 | 0.97804 |
| 24 | H4B | 5.6182 | −4.0489 | 1.5426 | 1.1700 | 0.97804 |

[a] All distances in bohr. In the azide monomer $x$ is rotated with respect to $x \parallel$ Cu–$N_4$.

**III.A.2. Ground-State Properties of the Azide Monomer and Dimer. a. Monomer.** The azide monomer model, $[Cu(NH_3)_3(N_3)]^+$ (model structure **1**), has an approximately square-planar coordination of ammonia ($N_1$, $N_2$, $N_3$) and azide nitrogen atoms ($N_4$ coordinating, $N_5$ central, $N_6$ terminal) around the central cupric ion with $C_s$ molecular symmetry. Energies and charge distributions of the one-electron energy levels from spin-unrestricted SCF–X$\alpha$–SW calculations are given in Table III. A diagram of these energy levels is presented in Figure 5, left. With the $x$-axis given by the vector Cu–$N_4$, the ground state of the molecule has one electron in the Cu $d_{x^2-y^2}$ spin-up orbital (level 18A′↑) and the corresponding $d_{x^2-y^2}$ spin-down orbital (level 18A′↓) is empty. Level 18A′↑ is the highest occupied (HOMO) and level 18A′↓ the lowest unoccupied molecular orbital (LUMO; cf. Table III). As shown in the contour plot of the wave function

(27) The ligand L′–O– is the anion of 2-([*N*,*N*-bis(2-pyridylethyl)-amino]methyl)phenol: Karlin, K. D.; Cohen, B. I.; Hayes, J. C.; Farooq, A.; Zubieta, J. *Inorg. Chem.* **1987**, *26*, 147–153.

(28) (a) Slater, J. C. *The Self-consistent Field for Molecules and Solids*; McGraw-Hill: New York, 1974; Vol. 4. (b) Johnson, K. H. *Adv. Quantum Chem.* **1973**, *7*, 143–185.

(29) (a) Noodleman, L.; Norman, J. G., Jr. *J. Chem. Phys.* **1979**, *70*, 4903–4906. (b) Noodleman, L. *J. Chem. Phys.* **1981**, *74*, 5737–5743.

(30) (a) Schwarz, K. *Phys. Rev. B* **1972**, *5*, 2466–2468. (b) Schwarz, K. *Theor. Chim. Acta* **1974**, *34*, 225–231.

(31) Transition energies (in eV) obtained by X$\alpha$ transition state calculations and experimental ionization energies (in parentheses) (from: Lee, T. H.; Colton, R. J.; White, M. G.; Rabalais, J. W. *J. Phys. Chem.* **1975**, *79*, 4845) are as follows: $1\pi_g$ 4.0 (4.0); $3\sigma_u$ 9.7 (8.0); $4\sigma_g$ 10.6 (9.5); $1\pi_u$ 9.3 (12.8); $2\sigma_u$ 23.7 (24.2); $3\sigma_g$ 27.5 (28.2); $2\sigma_g$ 392.4 (398.9); $1\sigma_{u/g}$ 410.53 (403.5). The $^1\Sigma_u$ and $^1\Delta_u$ states were calculated at 6.0 eV. Cf.: Fischer, C. R.; Kemmey, P. J.; Klemperer, W. G. *Chem. Phys. Lett.* **1977**, *47*, 545–549.

**Table III.** Energy Levels and Charge Decomposition for Monomer Model $[Cu(NH_3)_3(N_3)]^+$ [a]

| level | | energy (eV) | charge decomposn (%) Cu | $N_4$ | $N_5$ | $N_6$ | $N_1 - N_3$ | int[b] |
|---|---|---|---|---|---|---|---|---|
| 18A′(↓) | d (LUMO) | +0.2545 | 53 | 3 | 3 | 7 | 27 | 6 |
| 18A′(↑) | d (HOMO) | −0.2545 | 51 | 4 | 2 | 6 | 30 | 6 |
| 7A″(↓) | $(\pi^{nb})_v$ | −1.7434 | 27 | 26 | 1 | 28 | 0 | 17 |
| 7A″(↑) | $(\pi^{nb})_v$ | −1.9716 | 13 | 31 | 1 | 34 | 0 | 21 |
| 17A′(↓) | d | −2.2216 | 86 | 3 | 0 | 3 | 2 | 6 |
| 16A′(↓) | d | −2.3413 | 81 | 6 | 0 | 5 | 3 | 4 |
| 6A″(↓) | d | −2.4594 | 98 | 0 | 0 | 0 | 0 | 1 |
| 17A′(↑) | $(\pi^{nb})_\sigma$ | −2.6463 | 28 | 25 | 1 | 25 | 4 | 15 |
| 15A′(↓) | $(\pi^{nb})_\sigma$ | −2.6496 | 30 | 20 | 2 | 22 | 11 | 13 |
| 5A″(↓) | d | −2.7325 | 72 | 9 | 1 | 10 | 0 | 8 |
| 16A′(↑) | d | −2.8494 | 78 | 3 | 0 | 2 | 10 | 6 |
| 15A′(↑) | d | −3.1111 | 87 | 2 | 0 | 3 | 4 | 2 |
| 6A″(↑) | d | −3.1252 | 98 | 0 | 0 | 0 | 0 | 1 |
| 5A″(↑) | d | −3.2850 | 86 | 4 | 1 | 5 | 0 | 4 |

[a] Energies have been scaled such that 0 eV is between the HOMO and LUMO. [b] Intersphere contribution.

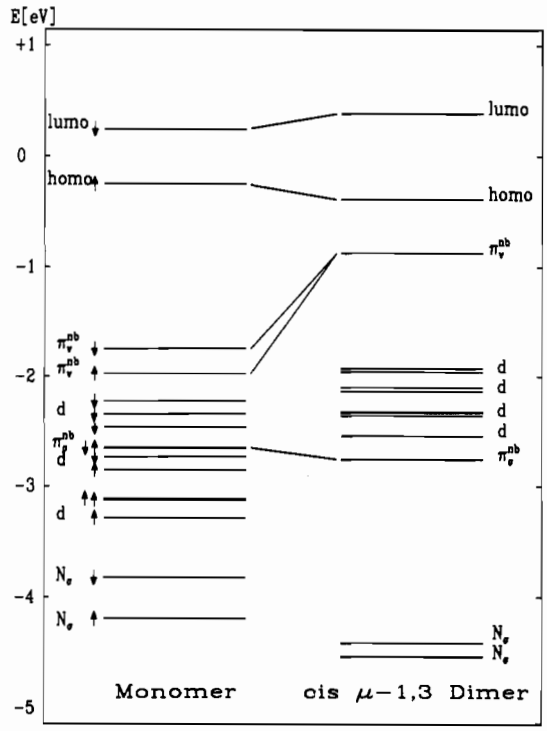


**Figure 5.** Energy levels of the Cu azide monomer (left) and dimer (right). The orbital energies have been scaled with 0 eV centered between the HOMO and LUMO.

of level 18A′↑ in Figure 6A, the Cu $d_{x^2-y^2}$ orbital is directed toward and delocalized on the neighboring ammonia and azide ligands and is antibonding with respect to the ligand valence orbitals. The HOMO and LUMO are split in energy by 0.5 eV as a result of the different spin-up and spin-down potentials. This splitting is only accounted for in a spin-unrestricted SCF calculation. The next levels at deeper binding energy are the azide $(\pi^{nb})_v$ spin orbitals (levels 7A″) oriented vertical to the Cu–$N_3$ plane. As shown in Table III, the azide $(\pi^{nb})_v$ orbital is equally distributed over both terminal nitrogens ($N_4$ and $N_6$) with vanishing contribution of the central nitrogen ($N_5$). The Cu contribution in the $(\pi^{nb})_v$↓ level is twice as large (27%) as in the $(\pi^{nb})_v$↑ level (13%), which induces an energy splitting of 0.2 eV between these levels. In contrast, the in-plane azide $(\pi^{nb})_\sigma$ spin-up and spin-down levels (levels 17A′↑ and 15A′↓) are close to degenerate. The contour plot of the wave function of level 17A′↑ (Figure 6B) shows that the $(\pi^{nb})_\sigma$ orbital is equally distributed over Cu and the terminal nitrogens $N_4$ and $N_6$ with vanishing contribution of the central nitrogen $N_5$ and that a $\sigma$ bonding interaction exists between Cu $d_{xy}$ and azide. This interaction stabilizes the $(\pi^{nb})_\sigma$ orbital by 0.8 eV below the energy of the $(\pi^{nb})_v$ orbital. The Cu $d_{xy}$ orbital in turn is destabilized by an antibonding interaction with the azide $(\pi^{nb})_\sigma$ orbital, which is, however, weaker than the overall metal–ligand antibonding interaction with $d_{x^2-y^2}$ such that

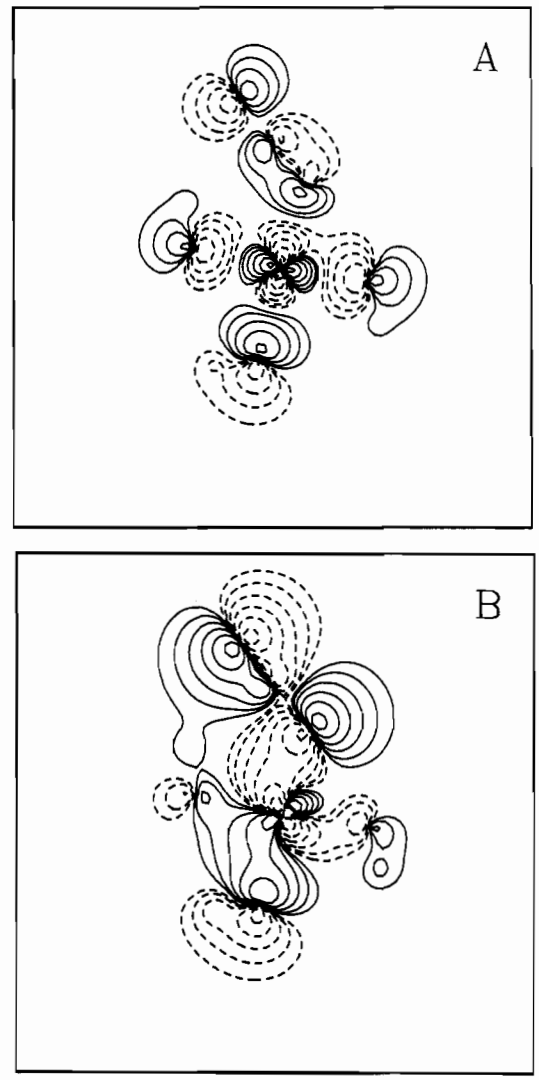


**Figure 6.** Contour plots of the Cu azide monomer in the $xy$ plane with the $x$-axis along the Cu–azide terminal N ($N_4$) bond: (A) HOMO; (B) $(\pi^{nb})_\sigma$. Contours are located at ±0.005, ±0.01, ±0.02, ±0.04, ±0.08, and ±0.16 $(e/bohr^3)^{1/2}$.

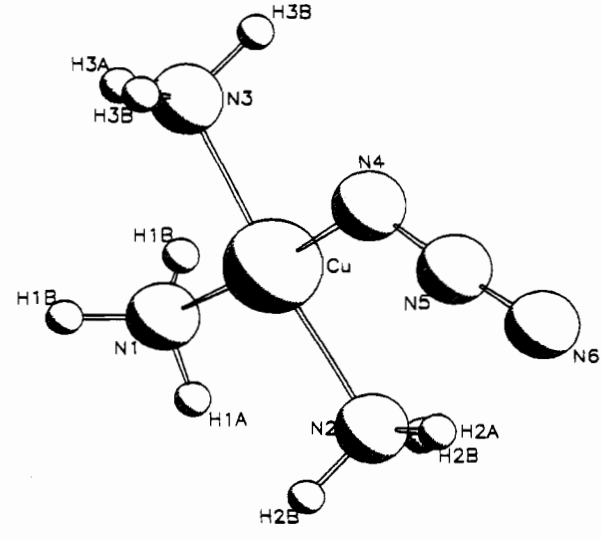


structure 1

**Table IV.** Energy Levels and Charge Decomposition for $[Cu_2(NH_3)_4(OH)(N_3)]^{2+}$

(A) Full Symmetry ($C_{2v}$) Calculation[a]

| level | | energy (eV) | charge decomposn (%) | | | | | |
|---|---|---|---|---|---|---|---|---|
| | | | $Cu_1(Cu_2)$ | $N_5(N_7)$[b] | $N_6$[c] | OH | $N_1,N_2(N_3,N_4)$[d] | int[e] |
| $13B_1$ | d (LUMO) | +0.3838 | 32 | 5 | 0 | 5 | 10 | 0 |
| $14A_1$ | d (HOMO) | −0.3838 | 35 | 1 | 3 | 1 | 11 | 0 |
| $5A_2$ | $(\pi^{nb})_v$ | −0.8704 | 8 | 32 | 2 | 0 | 0 | 18 |
| $6B_2$ | d | −1.9246 | 42 | 0 | 0 | 13 | 0 | 2 |
| $12B_1$ | d | −1.9531 | 39 | 7 | 0 | 0 | 1 | 4 |
| $13A_1$ | d | −2.0976 | 47 | 0 | 0 | 0 | 3 | 3 |
| $11B_1$ | d | −2.1338 | 46 | 2 | 0 | 0 | 1 | 1 |
| $12A_1$ | d | −2.3225 | 49 | 0 | 0 | 0 | 0 | 0 |
| $5B_2$ | d | −2.3287 | 49 | 0 | 1 | 0 | 0 | 1 |
| $4A_2$ | d | −2.3541 | 49 | 0 | 0 | 0 | 0 | 1 |
| $3A_2$ | d | −2.5411 | 43 | 4 | 0 | 0 | 0 | 4 |
| $10B_1$ | $(\pi^{nb})_\sigma$ | −2.7564 | 20 | 22 | 1 | 0 | 4 | 7 |

(B) Broken Symmetry ($C_s$) Calculation

| level | | energy (eV) | charge decomposn (%)[f] | | | | | | | |
|---|---|---|---|---|---|---|---|---|---|---|
| | | | $Cu_1$ | $Cu_2$ | $N_5$ | $N_6$ | $N_7$ | OH | $N_1,N_2$ | $N_3,N_4$ | int[e] |
| 27A′(↑) | d (LUMO) | +0.3846 | 31 | 34 | 5 | 0 | 4 | 5 | 9 | 10 | 0 |
| 26A′(↑) | d (HOMO) | −0.3846 | 36 | 33 | 1 | 3 | 1 | 1 | 12 | 11 | 0 |
| 11A″(↑) | $(\pi^{nb})_v$ | −0.8699 | 8 | 8 | 32 | 2 | 32 | 0 | 0 | 0 | 19 |
| 10A″(↑) | d | −1.1236 | 37 | 47 | 0 | 0 | 0 | 13 | 0 | 0 | 2 |
| 25A′(↑) | d | −1.9504 | 29 | 50 | 7 | 0 | 7 | 1 | 1 | 1 | 4 |
| 24A′(↑) | d | −2.0984 | 48 | 45 | 1 | 0 | 0 | 0 | 1 | 2 | 3 |
| 23A′(↑) | d | −2.1333 | 45 | 48 | 1 | 0 | 1 | 1 | 1 | 1 | 1 |
| 22A′(↑) | d | −2.3252 | 58 | 39 | 1 | 0 | 0 | 0 | 0 | 0 | 0 |
| 9A″(↑) | d | −2.3261 | 38 | 59 | 0 | 1 | 0 | 0 | 0 | 0 | 1 |
| 8A″(↑) | d | −2.3559 | 55 | 43 | 0 | 0 | 0 | 0 | 0 | 0 | 1 |
| 7A″(↑) | d | −2.5437 | 53 | 34 | 4 | 0 | 4 | 0 | 0 | 0 | 4 |
| 21A′(↑) | $(\pi^{nb})_\sigma$ | −2.7564 | 21 | 18 | 22 | 1 | 22 | 0 | 4 | 4 | 7 |

[a] Energies have been scaled such that 0 eV is centered between the HOMO and LUMO. [b] Terminal N of the azide group. [c] Central N of the azide group. [d] Ammonia nitrogens. [e] Intersphere contribution. [f] Atom designations and energy scaling as in part A.

the latter orbital is the HOMO (see above). In fact, $d_{x^2-y^2}$ is primarily antibonding with respect to the ammonia nitrogens ($N_1$–$N_3$) (see Table III). The 13% azide contribution to the HOMO 18A′↑ is mixed (see Figure 6A), i.e. a superposition of $-(\pi^{nb})_\sigma = -(1/\sqrt{2})[p(N_4) - p(N_6)]$ for the antibonding interaction of $d_{x^2-y^2}$ with $(\pi^{nb})_\sigma$ and $+(\pi^*)_\sigma = +(1/\sqrt{2})\,((1/\sqrt{2})[p(N_4) + p(N_6)] - p(N_5))$ for the bonding interaction with $+(\pi^*)_\sigma$; $p(N_i)$ are the in-plane nitrogen $p\pi$ orbitals of $N_4$, $N_5$, and $N_6$. The bonding interaction with the high-energy azide $\pi^*$ orbital corresponds to back-conation of electron density from the metal to the ligand, a feature not commonly associated with the azide ligand.[32]

**b. Dimer.** The dimer model used here has a square planar coordination for each cupric ion including ammonia nitrogens ($N_1$–$N_4$), a bridging hydroxo, and a cis $\mu$-1,3 bridging azide ($N_5$–$N_7$; $N_6$ central) ligation (model structure **2**). The molecular symmetry is $C_{2v}$. Energies and charge distributions of the one-electron levels from spin-unrestricted SCF–X$\alpha$–SW calculations are given in Table IVA, and the energy level diagram is presented in Figure 5, right. The contour plots of the wave functions are presented in Figure 7.

With the $x$-axis along the Cu–Cu vector (cf. Figure 1), the ground state of the azide dimer has two electrons in the half-occupied $d_{xy}$ orbitals of each copper. The HOMO (level $14A_1$) is the symmetric ($A_1$) combination of the $d_{xy}$ orbitals (see Figure 7B), and the LUMO (level $13B_1$) is the antisymmetric ($B_1$) combination with respect to the mirror plane between the two coppers (see Figure 7A). The $B_1$ combination of the $d_{xy}$ orbitals undergoes a $\sigma$ bonding–antibonding interaction with the in-plane ($\pi^{nb}$) azide orbital: the contour plot of level $10B_1$ (Figure 7C) shows the $\sigma$ bonding interaction between the $d_{xy}$ orbitals and the azide $(\pi^{nb})_\sigma$ level, and the contour plot of level $13B_1/27A'$ (LUMO; Figure 7A) shows the $\sigma$ antibonding interaction with $(\pi^{nb})_\sigma$. Table IVA indicates that level $10B_1$ is equally distributed over the two coppers and the two terminal nitrogens of the azide group, $N_5$ and $N_7$, with no contribution of the central nitrogen ($N_6$). This interaction is the primary contribution to the azide bond and lowers the $(\pi^{nb})$ level to −2.37 eV below the HOMO energy. The LUMO (level $13B_1$) is reciprocally raised in energy by the antibonding interaction (see Figure 5, right) to 0.77 eV above the HOMO energy. Figure 7A shows that the interaction of the Cu $d_{xy}$ is not only antibonding with respect to azide but also with respect to all other ligands, i.e. hydroxide and ammonia (cf. part a). In particular the hydroxide contribution in the LUMO (see Table IVA) acts to increase the HOMO–LUMO splitting. By symmetry, the HOMO (level $14A_1$) cannot interact with the azide $(\pi^{nb})_\sigma$ orbital and is primarily nonbonding. However, the contour plot of this level (Figure 7B) shows a contribution of the in-plane high-energy azide $(\pi^*)_\sigma$ orbital (cf. part a). Thus, the $(\pi^*)_\sigma$

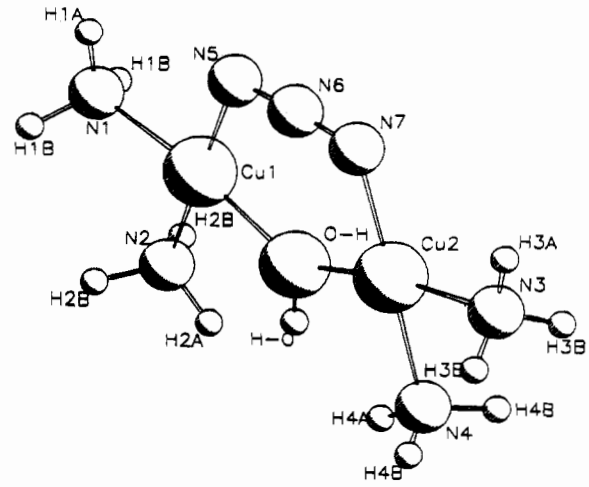


structure 2

(32) Jones, K. In *Comprehensive Inorganic Chemistry*; Pergamon Press: Oxford, U.K., 1973; Vol. 2, Chapter 19 (Nitrogen), pp 147–388.

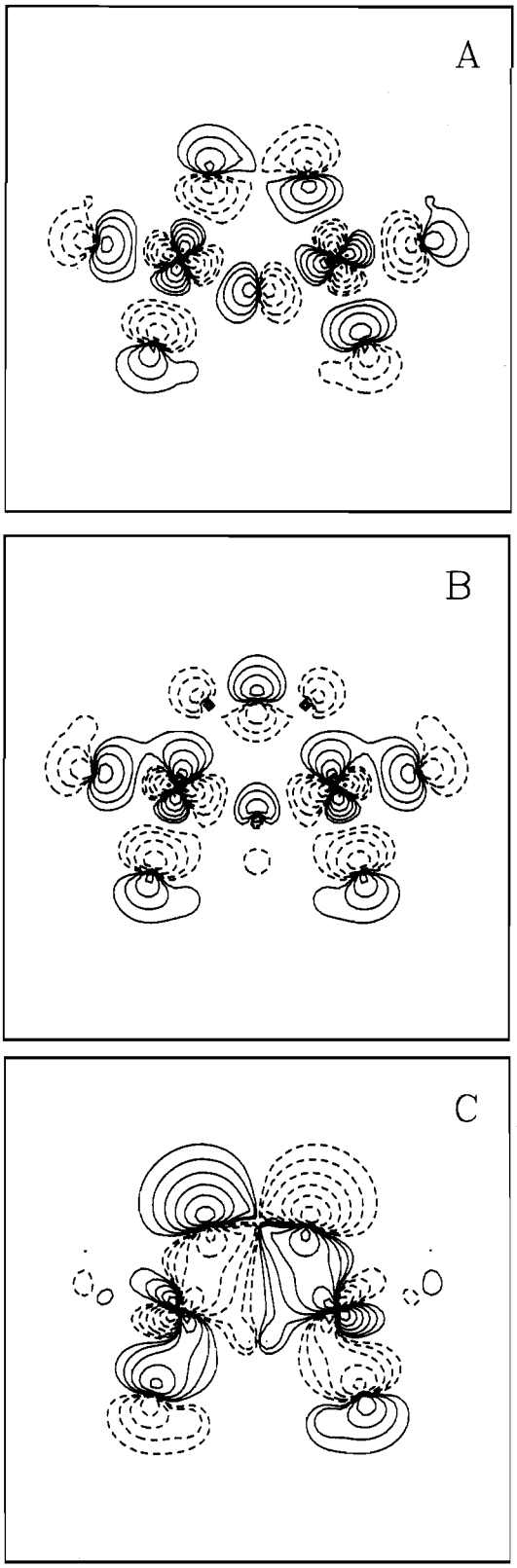


**Figure 7.** Contour plots of the Cu azide dimer in the $xy$ plane with the $x$-axis along the Cu–Cu vector: (A) LUMO; (B) HOMO; (C) $(\pi^{nb})_\sigma$. Contours are located at ±0.005, ±0.01, ±0.02, ±0.04, ±0.08, and ±0.16 e/bohr.

orbital which is unoccupied and lies at an energy of +3.968 eV above the HOMO acts to stabilize the HOMO with respect to the LUMO. Together these interactions lead to an increased HOMO–LUMO splitting and to a significant stabilization of the Cu–azide bond. As shown in Figure 5, right, and Table IVA, the next level below the HOMO at –0.5 eV consists primarily of the azide out-of-plane $(\pi^{nb})_v$ orbital weakly interacting with Cu. At deeper binding energy, but above the $(\pi^{nb})_\sigma$ orbital, are the remaining copper d levels.

**Table V.** Results of SCF–X$\alpha$ Transition-State Calculations, VBCI Parameters, and Optical Transition Energies (Rounded Values) for the Cu(II) Azide Dimer System[a] with All Energies in cm$^{-1}$ and Optical Transitions Given with Polarizations

| | MO (full sym), VBCI | MO (broken sym) |
|---|---|---|
| $^3B_1^{GS} \rightarrow {}^3A_1^{CT}$ | 26 681 | |
| $^3A_1^{CT} \rightarrow {}^3B_1^{CT}$ | 6 849 | |
| $\Delta$ | 19 832 | |
| $^3B_1^{GS} \rightarrow {}^3B_2^{CT} = \Delta_v$ | 10 674 | |
| $h_{d\pi}$ | –13 518 | |
| $E_{DCT}$ | 80 000 | |
| $U$ | 52 426[b] | |
| $\pi^*_\sigma$(lower) ($^1A_1^{GS} \rightarrow {}^1B_1^{CT}$) | 23 500 ($z$) | 30 900 |
| $\pi^*_\sigma$(higher) ($^1A_1^{GS} \rightarrow {}^1A_1^{CT}$) | 27 000 ($x$) | |
| $\pi^*_v$ ($^1A_1^{GS} \rightarrow$ ($^1B_2$, $^1A_2$)) | 19 300 ($y$, $R_x$, $R_z$) | 15 300 |
| $-2J^{GS}$ | 1 700 | 3 600 |
| $-2J^{CT}$ | 8 200 | |

[a] $x \parallel$ Cu–Cu, $C_2 = z$. [b] Experimental value.

**c. Antiferromagnetism of the Azide Dimer.** A theoretical value for the magnitude of the ground state magnetic coupling constant $-2J^{GS}$ can be obtained by calculating the energy difference between the ground-state triplet, $^3B_1^{GS}$, and the ground-state singlet, $^1A_1^{GS}$:

$$-2J^{GS} = E_{S=1} - E_{S=0} = E(^3B_1^{GS}) - E(^1A_1^{GS}) \quad (30)$$

In the framework of the X$\alpha$ calculation, excited-state energies can be estimated with the Slater transition-state method, where half an electron is transferred from a donating into an accepting orbital and after convergence the energy difference between the half-occupied orbitals is the transition energy.[28] For a spin-allowed transition, the electron is moved from an orbital of a given spin into an orbital of the same spin, and for a spin-forbidden transition it is moved into an orbital of opposite spin. A transition energy of $-2J$ = 3606 cm$^{-1}$ is obtained for the $^1A_1^{GS} \rightarrow {}^3B_1^{GS}$ transition.

Due to the incomplete description of the $^1A_1^{GS}$ ground state in the single-determinant MO wave function $^1\Phi_+^{GS}$ (cf. Table I, Scheme V in part II.B.2 and Discussion), the $-2J$ value obtained this way is in general too large. Alternatively, the calculation can be carried out in the broken-symmetry formalism,[29] which removes symmetry elements relating the two halves of the dimer. In the limit of weakly interacting dimers where the magnetic electrons are localized on each metal center, this broken-symmetry state $\Phi^{bs}$ is an equal mixture of the "correct" singlet wave function $^1\Psi_+^{GS} = {}^1A_1^{GS}$ (see Table I) and the triplet wave function $^3\Psi_-^{GS}$ ($M_S$=0) = $^3B_1^{GS}$ ($M_S$=0).[29] Hence, the energy of $\Phi^{bs}$ is the average of the (correct) singlet- and triplet-state energies, and the ground-state splitting is *twice* the energy difference of the triplet and broken-symmetry states

$$-2J^{GS} = 2[E_{S=1} - E_{S=0}] = 2[E(^3B_1^{GS}) - \langle\Phi^{bs}\rangle] \quad (31)$$

We find that the broken-symmetry calculation for the dimer gives no localization, i.e. the HOMO, LUMO, and azide $(\pi^{nb})$ spin-up and spin-down levels are equally distributed over both halves of the dimer (Table IVB). This means, $\langle\Phi^{bs}\rangle \geq \langle{}^1\Phi_+^{GS}\rangle$ and the full symmetry calculation is "stable" toward localization. Correspondingly, the broken-symmetry calculation of $-2J$ is found to give the same result as the full symmetry calculation (Table V). An alternative evaluation of $-2J^{GS}$ in terms of the VBCI model is given in section III.B.

**III.A.3. Excited-State Transition Energies.** The Slater-transition-state method has also been shown to provide a reasonable estimate of excited-state energies as it partially includes

**Scheme IX**

relaxation effects due to changes in the electron density distribution in the transition.[28a] This is particularly important when calculating charge-transfer (CT) transitions. Excited-state transition energies for the $(\pi^{nb})_\sigma$ and $(\pi^{nb})_v$ CT states are compiled in Table V. All calculations have been carried out both for the monomer and the dimer in the spin-unrestricted formalism. For the dimer, transition states were calculated in full ($C_{2v}$) as well as in broken symmetry ($C_s$).

First, the triplet state energies are evaluated in $C_{2v}$ symmetry. The transition from the triplet ground state $^3B_1^{GS}$ to the $(\pi^{nb})_\sigma$ CT triplet excited state $^3A_1^{CT}$ is effected by moving an electron from $(\pi^{nb})_\sigma$ to the HOMO (Scheme IX). The corresponding transition energy (see Table V) is calculated by converging the configuration with half a spin-down electron in $(\pi^{nb})_\sigma$ and half a spin-down electron in the HOMO (*vide supra*). Starting from the converged $^3A_1^{CT}$ state (cf. Scheme VIII, left), the transition energy to the $^3B_1^{CT}$ state (cf. Scheme VIII, right) is calculated by moving the half of a spin-down electron from the HOMO to the LUMO. Hence, the energy difference $E(^3B_1^{CT}) - E(^3A_1^{CT})$ = 6850 cm$^{-1}$ of the $(\pi^{nb})_\sigma$ states (see Table V) should approximately correspond to the HOMO–LUMO splitting (cf. (29)). This quantity was calculated independently by converging the ground-state triplet and taking the energy difference between the HOMO and LUMO which gives a value of 6727 cm$^{-1}$. In analogy with the $(\pi^{nb})_\sigma$ transition, the transition energy from the triplet ground state to the $(\pi^{nb})_v$ triplet CT state $^3B_2^{CT}$ is calculated by moving an electron from $(\pi^{nb})_v$ to the HOMO (cf. Scheme IX and Table V). In the following section, the azide → Cu CT energies are calculated with the VBCI model on the basis of the (full symmetry) triplet → triplet transition energies obtained in this section.

For comparison, excited-state transition energies have also been calculated in the broken-symmetry formalism and are included in Table V. Here, only $M_S = 0$ excited configurations with one electron shifted from $(\pi^{nb})_\sigma$ or $(\pi^{nb})_v$ to the LUMO are calculated giving, in the weak coupling regime, transition energies averaged over the singlet and triplet as well as over the $A_1$ and $B_1$ components of $(\pi^{nb})_\sigma$ and the $A_2$ and $B_2$ components of $(\pi^{nb})_v$, respectively.[21] The average transition energy from the broken symmetry ground state to the $(\pi^{nb})_\sigma$ CT state is 30 934 cm$^{-1}$ and to the $(\pi^{nb})_v$ CT state 15 300 cm$^{-1}$. Compared with the mean experimental $(\pi^{nb})_\sigma$ transition energy of 25 600 cm$^{-1}$, the broken-symmetry value of 30 934 cm$^{-1}$ is ~5000 cm$^{-1}$ too high. This corresponds to the observation made in our previous X$\alpha$ study of copper peroxo systems that the $(\pi^{nb})_\sigma$ transition energy obtained from a broken-symmetry transition-state calculation is systematically too high. In contrast, the $(\pi^{nb})_v$ energy is ~4000 cm$^{-1}$ too low if compared to a band observed at 19 000–20 000 cm$^{-1}$ in met azide hemocyanins and met apo hemocyanin which has absorption as well as CD intensity and has been assigned to the $(\pi^{nb})_v$ transition.[15]

**III.B. Valence-Bond–CI Model.** In section II.B it has been shown that the MO description of the ground and $(\pi^{nb})_\sigma$ CT excited triplets, $^3B_1^{GS}$, $^3A_1^{CT}$, and $^3B_1^{CT}$, coincides with the valence-bond–CI (VBCI) formalism. In terms of the VBCI model, the splitting of the triplet $(\pi^{nb})_\sigma$ CT state into $^3A_1^{CT}$ and $^3B_1^{CT}$ (see Table V) is due to configuration interaction (CI) between $^3B_1^{GS}$ and $^3B_1^{CT}$, while no interaction exists for $^3A_1^{CT}$ (cf. section II.B.1).

The $^3B_1$ secular problem is given by

$$\begin{array}{c|cc|} & \text{GS} & \text{CT} \\ \text{GS} & 0 & h_{d\pi} \\ \text{CT} & h_{d\pi} & \Delta \end{array} \qquad (32)$$

(cf. (17)), where $\Delta$ is the zeroth order CT energy, i.e. the energy difference between the unperturbed $^3B_1^{GS}$ and ($^3B_1^{CT}$, $^3A_1^{CT}$) states (see Figure 8, right). Note from Figure 8 that $^3B_1^{GS}$ is stabilized by the same amount as $^3B_1^{CT}$ is destabilized with respect to $^3A_1^{CT}$. Hence, with a value of 26 681 cm$^{-1}$ for $E(^3A_1^{CT}) - E(^3B_1^{GS})$ and 6849 cm$^{-1}$ for $E(^3B_1^{CT}) - E(^3A_1^{CT})$ (Table V), $\Delta$ is 26 681 − 6849 = 19 832 cm$^{-1}$ and the $^3B_1^{CT}$ state is at 26 681 + 6849 = 33 530 cm$^{-1}$ above the ground triplet (see Figure 8, "SCF triplets", and Table V). This mutual repulsion of the $^3B_1$ states is reproduced by a value of the transfer integral $h_{d\pi}$ of −13 518 cm$^{-1}$ in (36).

The values of $h_{d\pi}$ and $\Delta$ determined numerically from the triplet states are now used in the VBCI analysis of the singlet states. First the 2 × 2 $^1B_1$ problem (eq 23) is treated which involves the interaction of $^1B_1^{CT}$ with the metal-to-metal CT (MMCT) state, $^1B_1^{MMCT}$ (cf. Scheme III in section II.B.1). From photoelectron spectroscopy, the energy of the MMCT state, also known as the Mott–Hubbard $U$,[33] is known to be around 6.5 eV.[34] The $^1B_1$ interaction matrix

$$\begin{array}{c|cc|} & \text{CT} & \text{MMCT} \\ \text{CT} & \Delta - E & h_{d\pi} \\ \text{MMCT} & h_{d\pi} & U - E \end{array} \qquad (33)$$

leads to a mutual repulsion of 4877 cm$^{-1}$ between the $^1B_1$ states (see Figure 8, "$^1B_1$–CI"). Finally, the $^1A_1$ secular problem (eq 22) is solved. In addition to the interaction of the $^1A_1^{CT}$ state with the MMCT state of the same symmetry, there is also an interaction of magnitude $\sqrt{2}\,h_{d\pi}$ with the double CT (DCT) state (cf. Scheme IV in section II.B.1). The energy of this state, $E_{DCT}$, is here assumed to be identical with the second ionization energy of azide, $N_3^-$. From ab-initio Hartree–Fock calculations, the total energy of $N_3^+$ is ~80 000 cm$^{-1}$ above the total energy of $N_3^-$.[35] About the same value for $E_{DCT}$ (76 000 cm$^{-1}$) is obtained by moving the two electrons of $(\pi^{nb})_\sigma$ stepwise to the LUMO via the $^3A_1^{CT}$ triplet CT state. Using the above values in the $^1A_1$ secular determinant

$$\begin{array}{c|cccc|} & \text{GS} & \text{CT} & \text{MMCT} & \text{DCT} \\ \text{GS} & 0 & h_{d\pi} & 0 & 0 \\ \text{CT} & h_{d\pi} & \Delta & h_{d\pi} & \sqrt{2}h_{d\pi} \\ \text{MMCT} & 0 & h_{d\pi} & U & 0 \\ \text{DCT} & 0 & \sqrt{2}h_{d\pi} & 0 & E_{DCT} \end{array} \qquad (34)$$

one obtains the energies shown in Figure 8, "$^1A_1$–CI" column. The energy of the $^1A_1^{CT}$ state is less changed than the energy of the $^1B_1^{CT}$ state since the interaction with the ground-state and the MMCT $^1A_1$ components act in opposite directions. However, the additional interaction of the $^1A_1^{CT}$ with the DCT state reduces the splitting between $^1A_1^{CT}$ and $^1B_1^{CT}$, since no $^1B_1$ DCT state exists. After the introduction of complete CI for the $^1A_1$ and $^1B_1$ states, the energies of the CT states are in excellent agreement with the experiment: $^1B_1^{CT}$ is calculated to be at 23 537 cm$^{-1}$ (experiment: 23 800 cm$^{-1}$), and $^1A_1^{CT}$ at 27 016 cm$^{-1}$ (experiment: 27 400 cm$^{-1}$). The splitting between $^1A_1^{CT}$ and $^1B_1^{CT}$ is calculated to be 3479 cm$^{-1}$, which is also very close to the observed

(33) Anderson, P. W. *Phys. Rev.* **1959**, *115*, 2.
(34) Didziulis, S. V.; Cohen, S. L.; Gewirth, A. A.; Solomon, E. I. *J. Am. Chem. Soc.* **1988**, *110*, 250–268.
(35) Archibald, T. W.; Sabin, J. R. *J. Chem. Phys.* **1971**, *55*, 1821–1829.

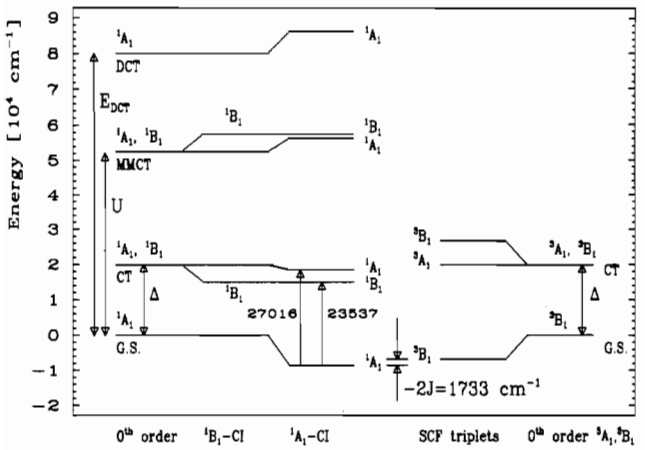


**Figure 8.** Energy level scheme resulting from application of the VBCI model for the $(\pi^{nb})_\sigma$ states of the Cu azide dimer.

value of 3600 $cm^{-1}$. In addition to this considerable improvement of the simple MO prediction of CT energies, the VBCI model gives a physical rationale for the excited-state antiferromagnetism: the MMCT and DCT transitions generating singlet, but not triplet, states cause a depression of the $A_1$, $B_1$ CT states by $\sim$10 000 $cm^{-1}$ relative to the triplets. As a measure of this interaction, we define

$$-2J^{CT} \equiv \langle(^3\Psi_-{}^{CT})'\rangle - \langle(^1\Psi_+{}^{CT})'\rangle \qquad (35)$$

From (35), we obtain a shift of $-2J^{CT} = 8217$ $cm^{-1}$ for the $^1A_1{}^{CT}$ below the $^3B_1{}^{CT}$ state. Via this depression of the CT singlets with respect to the CT triplets, the ground-state singlet is also lowered with respect to the ground-state triplet (cf. Figure 8). Thus, the VBCI treatment gives a coupling constant of $-2J^{GS} = 1733$ $cm^{-1}$, which is about half as large as the value of $-3600$ $cm^{-1}$ obtained from the SCF–X$\alpha$ transition-state calculation.

A similar treatment applies to the VBCI calculation of the $(\pi^{nb})_v \rightarrow$ Cu CT energies. As with the $(\pi^{nb})_\sigma$ states, the ground-state triplet $\rightarrow$ CT state triplet ($(\pi^{nb})_v \rightarrow$ HOMO; cf. Scheme IX) transition-state calculation gives the zeroth-order CT transition energy, which, in case of the $(\pi^{nb})_v \rightarrow$ Cu CT transition, is denoted by $\Delta_v$. In case of the [$Cu_2$(L–Et)($N_3$)] system, $\Delta_v$ has been calculated to 10 674 $cm^{-1}$ (Table V). Whereas the $(\pi^{nb})_\sigma$ state is split by CI with the ground state, no such interaction is possible for the $(\pi^{nb})_v$ state in planar symmetry. This is connected to the fact that, with respect to the molecular plane containing the Cu–$N_3$–Cu unit, $(\pi^{nb})_\sigma$ is symmetric and $(\pi^{nb})_v$ antisymmetric. Hence, no totally symmetric state derives from the $(\pi^{nb})_v$ CT state and, in terms of the VBCI model, there is no splitting of this CT state. Including the depression of the $^1A_1{}^{GS}$ ground state of 8582 $cm^{-1}$, the $(\pi^{nb})_v$ CT transition in terms of the VBCI model is therefore predicted at 19 256 $cm^{-1}$ ($^1B_2$, $^1A_2$), in good agreement with met azide hemocyanin data.[15] If the nonplanarity of the molecule is taken into account, a splitting of $(\pi^{nb})_v$ may result. In fact, the $C_{2v}$ symmetry assumed in our model calculation of the [$Cu_2$(L–Et)($N_3$)] dimer is an idealization (see section III.A.1).

## IV. Discussion

The model presented in this study has solved two conceptual problems which have emerged from spectroscopic[2d] and theoretical[21] investigations of peroxide- and azide-bridged copper dimers relevant to oxy-hemocyanin. The first problem was how to interpret the sign and magnitude of charge-transfer (CT) excited-state splittings observed in the optical spectra of these systems, as the TDVC (transition dipole vector coupling) model developed to interpret these CT spectra and determine the selection rules was shown to account for only a small fraction of the observed CT state splitting.[15] The second problem was related to the observation that bridging ligand $\rightarrow$ metal CT transitions in a dimer tend to be *lower* in energy than the corresponding transitions in the monomer whereas molecular orbital (MO) theory predicts the CT transition to be at *higher* energy in the dimer than in the monomer from the additional stabilization of the ligand valence orbital due to bridging. In this study, three models are developed and evaluated and it is shown that only the VBCI (valence-bond configuration interaction) model is able to explain the experimental CT spectra of structurally characterized copper(II) azide monomers and dimers.

The excitonic model takes into account only the diagonal electronic splittings expressed by the two-electron integrals $I$, $J_{d\pi}$, and $L$ (all positive) and the one-electron integral, $h_{AB}$ (see eqs 13 and 14). The $I$ contribution to the splitting can be estimated from the coupling of the CT transition moments (TDVC model), but this accounts in the case of the azide bridged dimer for only 10% of the observed splitting.[15] From exciton theory, it is known that the two-electron integral $L \ll I$;[23,36] hence, only $h_{AB}$ remains to account for the majority of the observed CT state splitting. The one-electron contribution $h_{AB}$ is, however, also anticipated to be small due to the large distance between the two copper centers. Apart from $h_{AB}$, the CT splitting scheme of the excitonic model is formally identical with the excited-state interaction scheme of two closed-shell molecules (four electrons, four orbitals) as derived by Robinson and El Sayed.[26] The physical difference is the fact that, in the case of the CT state of a metal dimer, one orbital containing one unpaired electron (bridging orbital) is shared by the two interacting centers whereas, for a dimer consisting of subunits being closed-shell in the ground state, no such overlap exists for any of the two singly occupied orbitals in the locally excited state. Both splitting schemes differ qualitatively from the splitting scheme for the d–d states of two coupled Cu(II) centers as derived for copper acetate.[5] The latter interaction scheme involves the same integrals, but only two electrons (or holes) are included in the dimer functions.

As the electronic splittings derived from the diagonal energies are too small to account for the observed values, off-diagonal terms have to be considered. In terms of the VBCI model, the CT state splitting results from configuration interaction (CI) of the "+" singlet CT component with the "+" singlet ground state, and the "–" triplet CT component with the "–" triplet ground state ("+" and "–" denote the transformation behavior with respect to the mirror plane between the two Cu centers of the cis $\mu$-1,3 azide dimer). Insight into the physical origin of the VB interaction is provided by a comparison with the CT splitting energy obtained in the MO model. It is shown that the triplet CT splitting in terms of the MO model is (i) given by the HOMO–LUMO-splitting energy and is (ii) identical to the triplet CT splitting obtained by the VBCI model. A similar splitting of a CT transition due to orbital splitting has been suggested for cobalt–superoxo dimers.[7] As the triplet ground-triplet CT state interaction is identical to the singlet ground-singlet CT state interaction, the VBCI singlet CT splitting is also given by the HOMO–LUMO-splitting but inverted relative to the triplet CT state splitting. This is, however, correct only to a first approximation since the singlet CT states interact with two additional states, the metal $\rightarrow$ metal CT (MMCT) and the double CT (DCT) states. The interaction of the "+" and "–" singlet CT with the "+" and "–" MMCT states acts to lower the energy of the singlet CT states below that of the triplet CT states and thus corresponds to an antiferromagnetic interaction. This excited-state antiferromagnetism (ESAF) is very large due to the direct interaction with the MMCT states ($\sim$10 000 $cm^{-1}$ in case of the azide dimer) and is the reason for the observation that CT bands in bridged dimers are at much lower energy than in the corresponding monomers. Thus, the "dimer bands" mentioned earlier derive from CT

transitions which are at high energy in the monomer but appear at much lower energy in the dimer due to ESAF. In general, antiferromagnetism is ascribed to spin pairing in overlapping orbitals; in fact, this approach corresponds to the usual VB concept.[36] We have alternatively started from orthogonal orbitals and introduced antiferromagnetism by CI. Both approaches are, of course, equivalent. In any case, the magnitude of ESAF depends on metal–ligand overlap as expressed by the transfer integral $h_{d\pi}$ (*vide infra*). As the HOMO–LUMO splitting and thus the CT excited-state splitting also depend on metal–ligand overlap, both the excited-state splitting and antiferromagnetism have the same physical origin. Finally, the "+" singlet CT state additionally interacts with the DCT state ("+" symmetry), which lowers the magnitude of the singlet CT state splitting somewhat but does not change the picture qualitatively.

The first direct evidence for ESAF was found in a study of $[Cu_2Cl_6]^{2-}$ systems some years ago.[24] Here, CT excitation at one Cu center creates a hole in a chlorine type MO extending over the four $Cl^-$ atoms coordinated to that copper which has good overlap with the singly occupied d orbital on the second copper. Hence, the singlet CT state is lowered by an energy > 3000 $cm^{-1}$ below the corresponding triplet CT state. As the condition for ESAF is the presence of unpaired electrons in a metal center, the Cu(II) dimers considered thus far may be contrasted to closed-shell dimers, e.g. Co(III) peroxo systems.[37] The comparison between the trans $\mu$-1,2 Cu peroxo and the analogous Co system is particularly interesting, as the $\pi^*_v$–$\pi^*_\sigma$ separation is only 2500 $cm^{-1}$ in the Cu(II), but 17 000 $cm^{-1}$ in the Co(III) case. As the $\pi^*_v$ state is not subject to ESAF (i.e. it does not provide an effective superexchange mechanism), the reason for this difference is strong ESAF in the $\pi^*_\sigma$ $^1$CT state of the Cu dimer but not the Co dimer. This in turn is due to the fact that excitation from the stable $d^6$–$d^6$ low-spin configuration to the $Co^{2+}$–$Co^{4+}$ MMCT configuration requires a much higher energy than to the $Cu^+$–$Cu^{3+}$ configuration in the Cu $d^9$–$d^9$ dimer. In addition, the MMCT configuration should be high spin and thus not interact with the singlet CT state.

The VBCI model is applied to a structurally characterized Cu cis $\mu$-1,3 azide bridged dimer giving a splitting of the $(\pi^{nb})_\sigma \rightarrow$ Cu CT transition into two transitions at 23 500 ($^1B_1$) and 27 000 $cm^{-1}$ ($^1A_1$), respectively, in close agreement with the observed values (23 800 and 27 400 $cm^{-1}$, respectively). The $(\pi^{nb})_\sigma \rightarrow$ Cu CT energy of the corresponding structurally characterized monomer is calculated at 27 815 $cm^{-1}$ (experimental value 25 600 $cm^{-1}$ [15]). Thus, the calculation also reproduces the experimental observation that the lower energy dimer CT transition is shifted to lower energy as compared with the parent monomer transition. In contrast, the broken-symmetry MO formalism applied to the cis $\mu$-1,3 azide dimer predicts an average $(\pi^{nb})_\sigma$ CT transition energy of 31 000 $cm^{-1}$, i.e. an overall shift of the CT transition to higher energy as compared to the monomer. The discrepancy to the VBCI prediction derives from the neglect of the CT splitting and, more importantly, the neglect of excited-state antiferromagnetism, which, in case of the azide dimer, amounts to 8000 $cm^{-1}$ (Table V). Finally, also the VBCI prediction of the $(\pi^{nb})_v$ transition energy (19 300 $cm^{-1}$) is superior to the broken-symmetry value (15 000 $cm^{-1}$) in comparison to spectral data.[15]

The electronic interactions present in the excited states of dimers are also of importance with respect to their ground-state properties which have been studied intensively.[1,3] As described in sections II.B.1 and III.B, ground-state antiferromagnetism (GSAF) results from the interaction of the ground-state singlet with the CT excited singlet lowered in energy due to ESAF. In a perturbation limit, we obtain from (17), (22), (30), and (35)

$$-2J^{CT} = h_{d\pi}{}^2\left(\frac{1}{U} + \frac{1}{E_{DCT}/2}\right) \tag{36}$$

and

$$-2J^{GS} = \frac{h_{d\pi}{}^4}{\Delta^2}\left(\frac{1}{U} + \frac{1}{E_{DCT}/2}\right) \tag{37}$$

With (28), (37) is the familiar expression for GSAF[38]

$$-2J^{GS} = \Delta E_{HL}{}^2\left(\frac{1}{U} + \frac{1}{E_{DCT}/2}\right) \tag{38}$$

but with an additional antiferromagnetic term $(E_{DCT}/2)^{-1}$ due to interaction of the singlet ground state with the DCT state. The example of the azide dimer shows that this term which appears in the VBCI and cluster–CI models[39,40] but is not accounted for by Anderson theory[41] is not negligible with respect to the familiar $1/U$ term. Further, with the ground state–CT state mixing coefficient $\lambda = -h_{d\pi}/\Delta$, a comparison of (36) and (37) gives

$$-2J^{GS} = \left(\frac{h_{d\pi}}{\Delta}\right)^1(-2J^{CT}) = \lambda^2(-2J^{CT}) \tag{39}$$

showing that GSAF results from ESAF by mixing of the ground with the CT excited state (cf. (18) for the triplets). A parallel result has been derived by Anderson,[42] but he has treated CT excited-state antiferromagnetism in a spin-Hamiltonian formalism. From realistic values of $\lambda$ (0.1–0.3), ESAF can be 1–2 orders of magnitude larger than GSAF. In case of the azide dimer, the VBCI model gives $-2J^{GS} \approx 1700$ $cm^{-1}$ (cf. Figure 8).

In summary, the present study has shown that the shift and splitting of a CT transition in a bridged dimer can be understood quantitatively by considering configuration interaction between ground and CT valence bond configurations. For an exact treatment, these effects have to be complemented by the splittings derived in section II, which can be described in terms of the two-electron integrals $L$ and $I$. The overall shift of a dimer CT transition to lower energy as compared to the monomer transition corresponds to excited-state antiferromagnetism (ESAF), which is due to the coupling of an unpaired electron in a ligand with an unpaired electron in a metal orbital. The CT state splitting provides a measure for the HOMO–LUMO splitting of the complex. Both effects can be used to obtain information about the magnitude of the transfer integral $h_{d\pi}$, i.e. about bonding in the complex. In principle, this information is also contained in the ground-state antiferromagnetism (GSAF) but only via admixture of the CT states. Hence, GSAF can be orders of magnitude smaller than ESAF. In the absence of direct overlap, a superexchange pathway via bridging ligand orbitals is required in order to provide a coupling between the two metal centers in the ground state. Since the intermediate states involved in these processes are exactly the CT states investigated here, we obtain also direct information on superexchange pathways in the electronic ground state of dimers. Thus, the spectroscopic investigation of a bridged dimer potentially provides a complete picture of the electronic structure, which is also of relevance for a detailed understanding of its ground-state magnetic properties.

**Acknowledgment.** E.I.S. thanks the NIH (Grant DK-31450) for support of this research. F.T. acknowledges the Deutsche Forschungsgemeinschaft (DFG) for a postdoctoral fellowship and Dr. Peter Adler, Stuttgart, Germany, for useful discussions.

(36) (a) Pilar, F. L. *Elementary Quantum Chemistry*; McGraw-Hill: New York, 1968. (b) Tinkham, M. *Group Theory and Quantum Mechanics*; McGraw-Hill: New York, 1964.
(37) Tuczek, F.; Solomon, E. I. *Inorg. Chem.* **1992**, *31*, 944–953.
(38) Hay, P. J.; Thibeault, J. C.; Hoffmann, R. *J. Am. Chem. Soc.* **1975**, *97*, 4884–4899.
(39) (a) Zaanen, J.; Sawatzki, G. A. *Can. J. Phys.* **1987**, *65*, 1262–1271. (b) Sawatzki, G. A. *Int. J. Mod. Phys. B* **1988**, *1*, 243–266.
(40) Shen, Z.-X.; Allen, J. W.; Yeh, J. J.; Kang, J.-S.; Ellis, W.; Spicer, W.; Lindau, I.; Maple, M. B.; Dalichaouch, Y. D.; Torikachvili, M. S.; Sun, J. Z.; Geballe, T. H. *Phys. Rev. B* **1987**, *36*, 8414–8428.
(41) Anderson, P. W. *Solid State Phys.* **1963**, *14*, 99–214.
(42) Anderson, P. W. *Phys. Rev.* **1950**, *79*, 350–356.